Stresses Associated with Subchondral Bone Cysts – A Finite Element Analysis on an Extended Stifle Joint

By

Lance Lamont Frazer

Submitted to the graduate degree program in Bioengineering and the Graduate Faculty of the University of Kansas in partial fulfillment of the requirements for the degree of Master of Science.

_____

Chairperson Dr. Kenneth Fischer

_____

Dr. Elizabeth Santschi

_____

Dr. Suzanne Shontz

Date Defended: April 29th, 2016

The Thesis Committee for Lance Lamont Frazer

certifies that this is the approved version of the following thesis:

Stresses Associated with Subchondral Bone Cysts – A Finite Element Analysis on an Extended Stifle Joint

_____

Chairperson Dr. Kenneth Fischer

Date approved: April 29th, 2016

Acknowledgement

Some days, 24 hours is too much to stay put in, so I take the day hour by hour, moment by moment. I break the task, the challenge, the fear into small, bite-size pieces. I can handle a piece of fear, depression, anger, pain, sadness, loneliness, illness. I actually put my hands up to my face, one next to each eye, like blinders on a horse. – Regina Brett

I would like to extend my sincere gratitude to my advisor at the University of Kansas, Dr. K. J. Fischer for allowing me to work under him. His patience, resources, persistent help and insight have not only made this research possible, but have allowed me to learn and grow as a young man. I would also like to extend the same bit of gratitude towards my co-advisor at Kansas State University, Dr. E. Santschi. Working under her toward the solution of a real-world, clinical problem has been invaluable. Her constant availability, openness, and extensive knowledge created a rich learning environment that fostered my success. I thank Dr. S. Shontz for being a part of my committee and providing expertise in computational modeling. I am grateful for the Bioengineering Graduate program here, namely Denise Bridwell, my friends, peers, colleagues, and everyone at the University of Kansas that has had a hand in my degree progress. None of this would be possible without the incredible support that each and every one of you provide. I thank my family for the constant love and support, and most importantly, my wife, who has been an anchor through the stormiest of days.

Abstract

Subchondral cystic lesions (SCL), sometimes referred to as subchondral bone cysts (SBC) or subchondral lucencies, occur in the medial femoral condyle (MFC) of horses and can cause lameness. They are more common in horses ≤ 2 years of age, but can occur in older horses. The causes of SCL are not well understood, however, trauma and osteochondrosis are most commonly implicated. Radiographs of young horses that develop SCLs indicate a progression from sclerosis to MFC flattening, and then a defect (SCL) that enlarges. Treatments are directed at reducing local inflammation and promoting bone and cartilage healing, with approximately 50-75% of horses becoming sound enough for work. However, bone healing after surgery is inconsistent, occurring in <20% of patients. Recently, a treatment of MFC SCL using a lag screw was reported to improve the rate of lameness resolution and is the first study to report significant and consistent bone healing. This suggests a biomechanical approach can improve the treatment of equine SCL, but very little is known about the stresses within the equine stifle and how the surgical procedure may be optimized. The equine stifle is a complex biological system and direct collection of biomechanical data would be difficult, if not impossible. The objective of this current study is to investigate the stresses in the subchondral femoral bone at different stages of cyst progression using finite element analysis. This information can help us better understand the mechanics associated with SCLs that will allow clinicians to develop and implement rational treatment strategies.

Table of Contents

Table of Figures

1. Introduction

"It's time… [to] take action to protect a species that has so loyally served humankind" – Jane Velez-Mitchell.

1.1. Stifle Joint Anatomy

The equine stifle joint is complex and provides motion and load transfer between the femur, the tibia and patella of the horse. The stifle's main functions are to allow flexion-extension motion with little resistance, efficiently transfer loads between the femur and tibia, and provide the structural support and mobility to allow the hindquarter muscular energy to be converted into powerful locomotion. There are three separate joints in the stifle; a femoropatellar and two femorotibial joints (medial and lateral). The stifle is supported by musculature, tendons, ligaments, and a joint capsule. Its stability and strength, paired with a large range of motion, make it an anatomical wonder. And rightly so, the stifle can propel a 454 kg racehorse at rates approaching 15 m/sec, and provide the power to an 800 kg draft horse to move five times its body weight. Unfortunately, because of the mechanical demands on the equine stifle, it is often a site of injury causing lameness, which can be severe enough to cause serious concerns. Thus, for the viability of the animal, it is of great importance to fully understand the relationship between the structure and function of the stifle joint, how this relationship can become compromised, and what veterinarians can do to treat pathologic joints with the most rational approach.

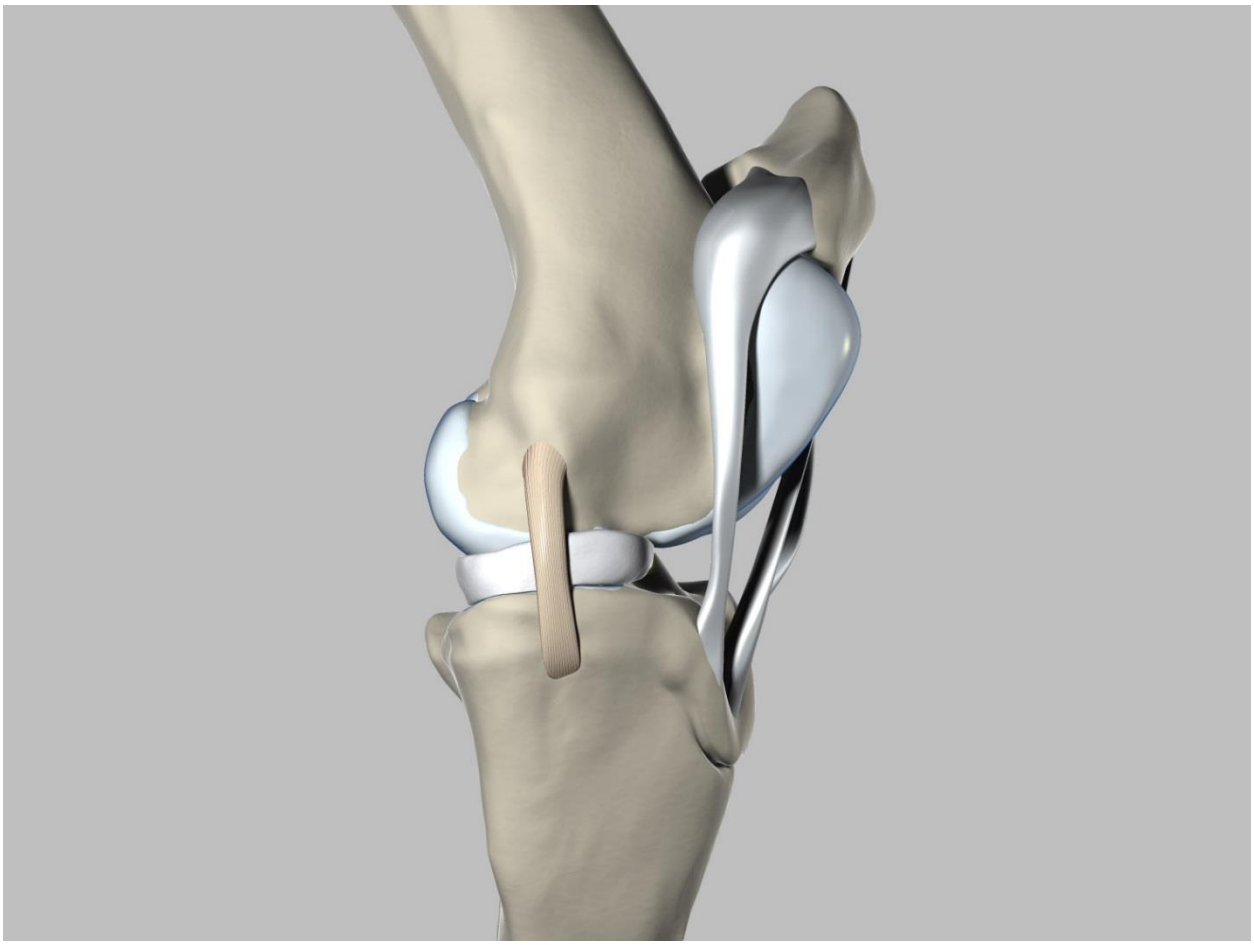

Figure 1.1 Idealized illustration of an equine stifle joint created by Tim Vojt. Shown are the major structures such as the femur, tibia, patella, meniscus, patellar ligaments, and a collateral ligament.

1.1.1. Anatomical Planes and Directions

Before each structure of the stifle is described, it's important to understand anatomical terms that provide spatial reference. These terms describe:

1) Two dimensional planes: these designations can be different for horses (and other quadrupeds) as compared to human anatomical planes. The three anatomical planes

are frontal (coronal for humans)), sagittal (lateral), and transverse (dorsal) (Figure 1.2).

2) Relative directions: For example, describing an anatomical structure as being to the "left" of another structure doesn't provide enough information because "left" would change depending on your perspective. Instead, choose to describe that same structure relative to anatomical locations, such as being more medial, meaning more towards the middle of the body. This anatomical direction wouldn't change depending on the point of reference. The most useful directional terms associated with the stifle joint are 1) cranial/caudal (anterior/posterior in human anatomy), which describes the direction from head to tail, 2) proximal/distal, which describes position relative to the spine with distal being further away and proximal being closer, 3) medial/lateral, where medial is closer to the middle of the horse, and finally 4) axial/abaxial, which refers to the central axis of the limb (Figure 1.2).

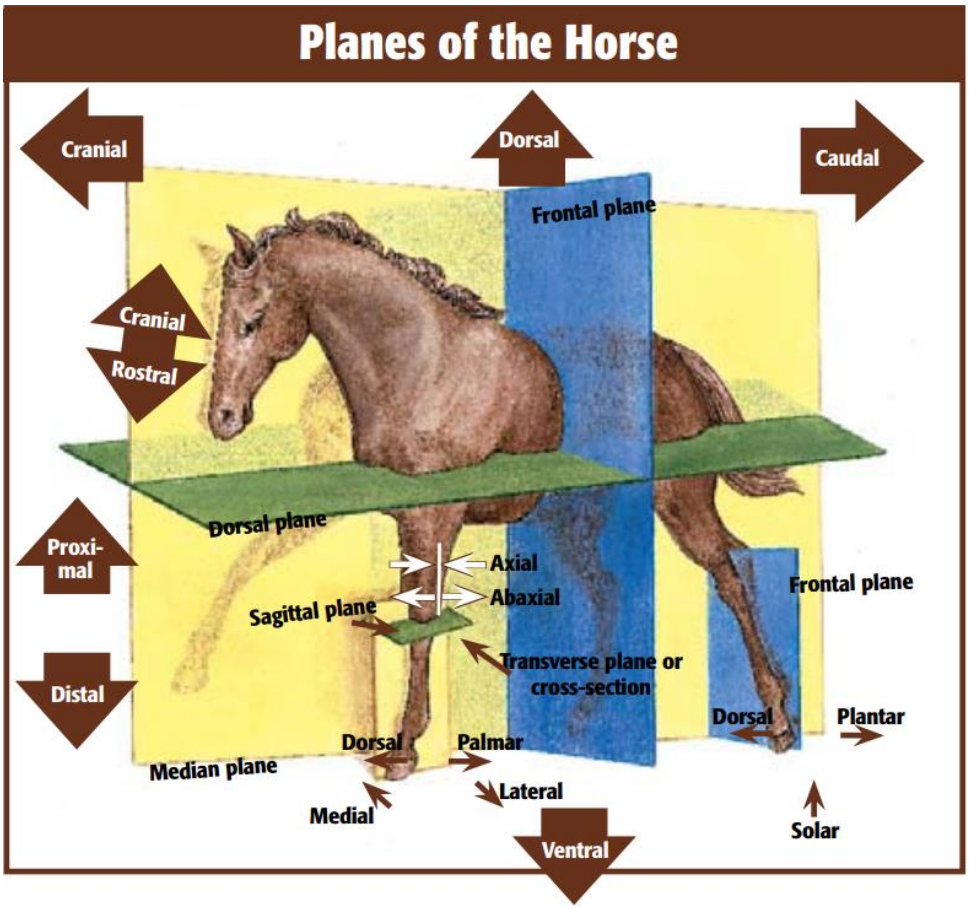

Figure 1.2 Diagram of a horse indicating all planes and directional terms for spatial reference.

© Les Sellnow

1.1.2. Bones

The three bones that make up the stifle joint are the femur, tibia, and patella. Colloquially known as the thigh bone, the femur is the largest bone in the horse (Figure 1.3). The distal end of the femur has two rounded condyles, the medial femoral condyle (MFC) and the lateral femoral condyle (LFC), which articulate with each side of the tibia forming the femorotibial joint. The medial femoral condyle is a common site for injury, more specifically, the most common site of bone cysts (see *Equine Bone Lesions)*. Proximally and cranially on the femur are two trochlear

ridges that provide the articulation with the patella. Another important part of the femur, the trochlear ridges (especially the lateral) tends to be another common site of injury. These injuries typically include osteochondrosis (radiographically seen as a loose piece of broken off femur), and/or osteochondrotic lesions.

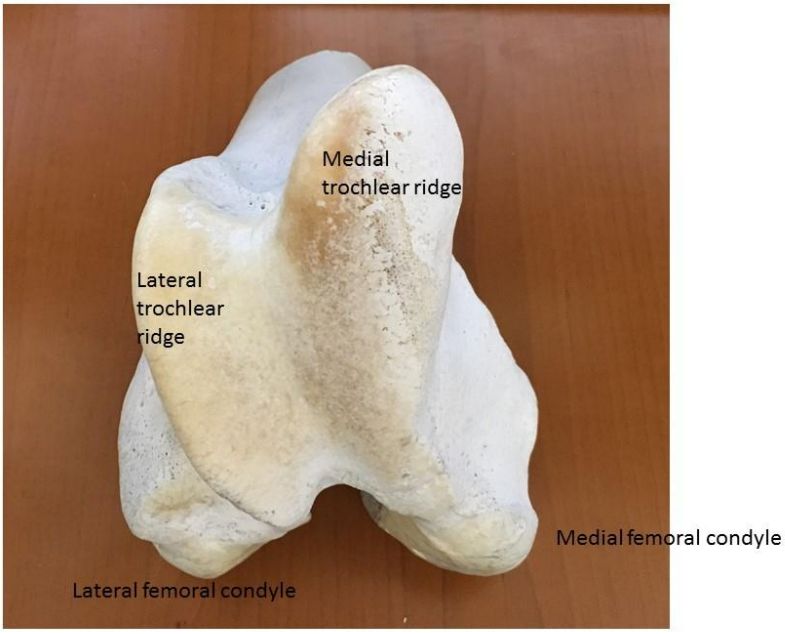

Figure 1.3 Cranial view of the femur showing the two condyles and the two trochlear ridges on the cranial side of the bone. These four structures are common sites for bone defects, with the medial trochlear ridge and medial condyle being the most common. Some such defects can cause complete lameness.

Colloquially known as the shin bone, the tibia, located distal to the femur, has a simpler geometry with two relatively flat plateaus at the proximal end, separated by two central ridges, the lateral and medial intercondylar eminences (Figure 1.4). Compared to the femur, the tibia

experiences less traumatic injury, yet is still subject to subchondral injury including bone cysts (sometimes in conjunction with a femoral cyst).

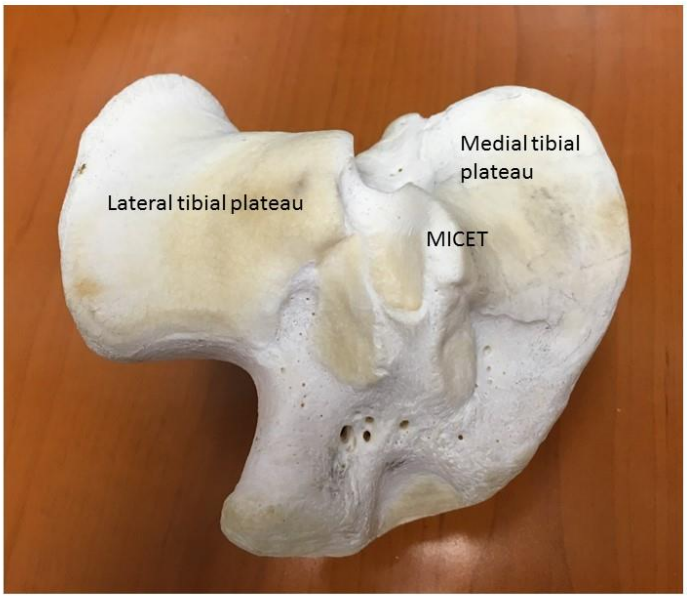

Figure 1.4 Dorsal view of the tibia showing each tibial plateau and the medial intercondylar eminence on the tibia (MICET).

Colloquially known as the knee cap, the patella articulates with the femur to form the femoropatellar joint. The patella, via the quadriceps muscles and coupled with the distal patellar ligaments, provides powerful stability to the femur and stifle joint and increases the moment arm of the quadriceps. The patella is subject to fractures, usually as a result of the horse competing in a jumping discipline (i.e, Eventing, Hunter/Jumper). These horses often strike their stifles against fences causing a large variety of fractures.

1.1.3. Cartilage

The articular cartilage of each bone is ~1-5 mm thick. This soft tissue provides some compliance under high force and protects the bones from shearing forces during motion under load. Cartilage with the synovial fluid has one of nature's lowest coefficients of friction. The low friction arises from cartilage's unique biological organization. Thus, cartilage allows two bones which it covers to move relative to each other without resistance (Figure 1.5). This unique biological organization also allows cartilage to handle the high load transfer across the joint. Articular cartilage is made up of water, Type II collagen, proteoglycans, chondrocytes, and other proteins. These components are organized differently depending on the depth through the thickness of the cartilage. To provide a frictionless, smooth surface, structures near the surface are organized perpendicular to the line of loading. Deeper to the articular surface, structures are organized parallel to the line of loading. The charge density of PGs, the water bound in PG, and intertwining of PG and collagen provide compressive strength to transfer load through the cartilage to the bone tissue. Cartilage is, for the most part, non-vascularized, which makes it a structure susceptible to slow healing in the event of trauma. It is common for veterinarians to observe cartilage defects in conjunction with bone defects. In adults, cartilage has a very limited capacity to heal as compared to bone. There is an intimate biomechanical interplay between cartilage and the bone that supports it (subchondral). Injury to one component almost always includes concomitant, or subsequent injury to the other. There is still debate whether OA starts in cartilage or subchondral bone.

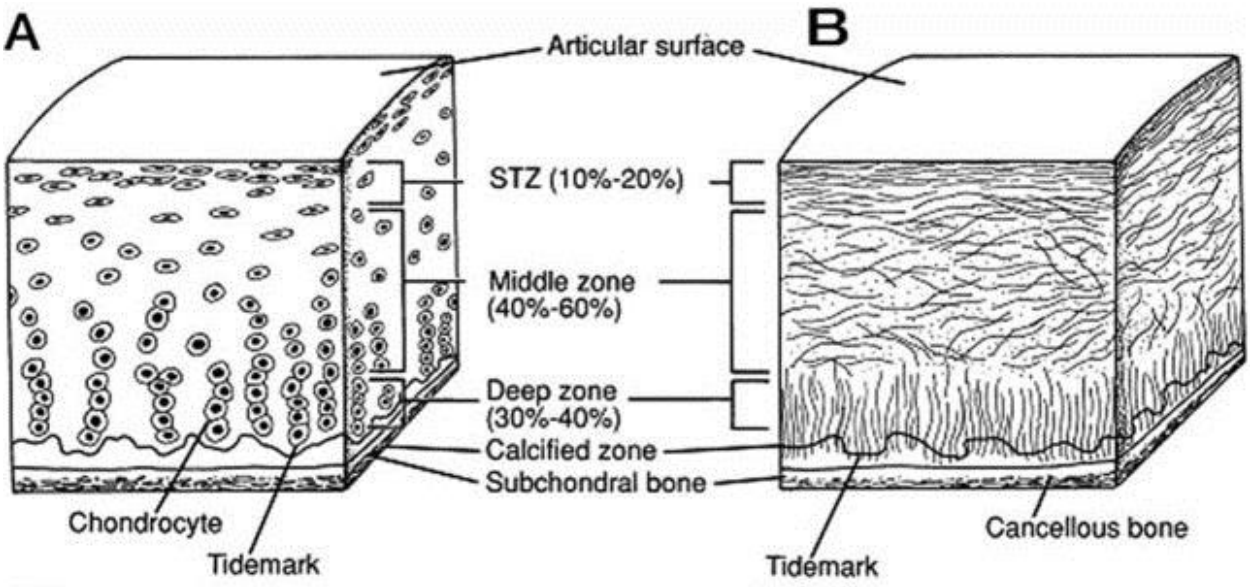

Figure 1.5 *Cross-sectional diagram showing the hierarchal structure of healthy articular cartilage. A: cellular organization; B: collagen organization.* Reprinted from the Journal of the American Academy of Orthopaedic Surgeons, 1994; 2:192-201 with permission.

1.1.4. Menisci

Interposed between the femur and tibia on the abaxial surface of both femoro-tibial joints is a crescent-shaped meniscus (Figure 1.6). The primary function of the meniscus is to convert compressive forces into circumferential hoop stresses, dissipating a large fraction of the load coming from the femur before reaching the tibia. It also provides some geometric constraint in the transverse plane. The meniscus has a composition similar to that of cartilage, but it is arranged differently so as to allow it to effectively dissipate the load. The meniscus is mostly comprised of water (72%) with the remainder being organic matter (collagen and proteoglycans). However, the organic matter gives the meniscus its unique properties. Aligned circumferentially, collagen fibers within the meniscus provide strength and support to handle the resulting hoop stress. Proteoglycans provide compressive strength. Because of this highly organized, aligned

structure, the meniscus has different properties depending on the direction of force (axial, radial, or circumferential). This is an important aspect to consider for computational modeling. The meniscus is susceptible to tears, especially at the inner ring, and is also susceptible to damage from an irregular condylar surface.

A common, emerging theme among veterinarians is that they often observe injuries that are concomitant or a result of another injury. The initial injury often goes untreated, as a horse may not show obvious lameness. This injury then leads to further injury in a cascade fashion, and a horse can quickly go from a slightly abnormal gait to complete lameness. Though it may seem like a chicken and egg dilemma, this cascading of injuries can be better understood by thorough study of more clinical cases by veterinarians, and also by computational modeling of the injuries. Through modeling an injury, one can examine how other anatomical structures are affected by the injury.

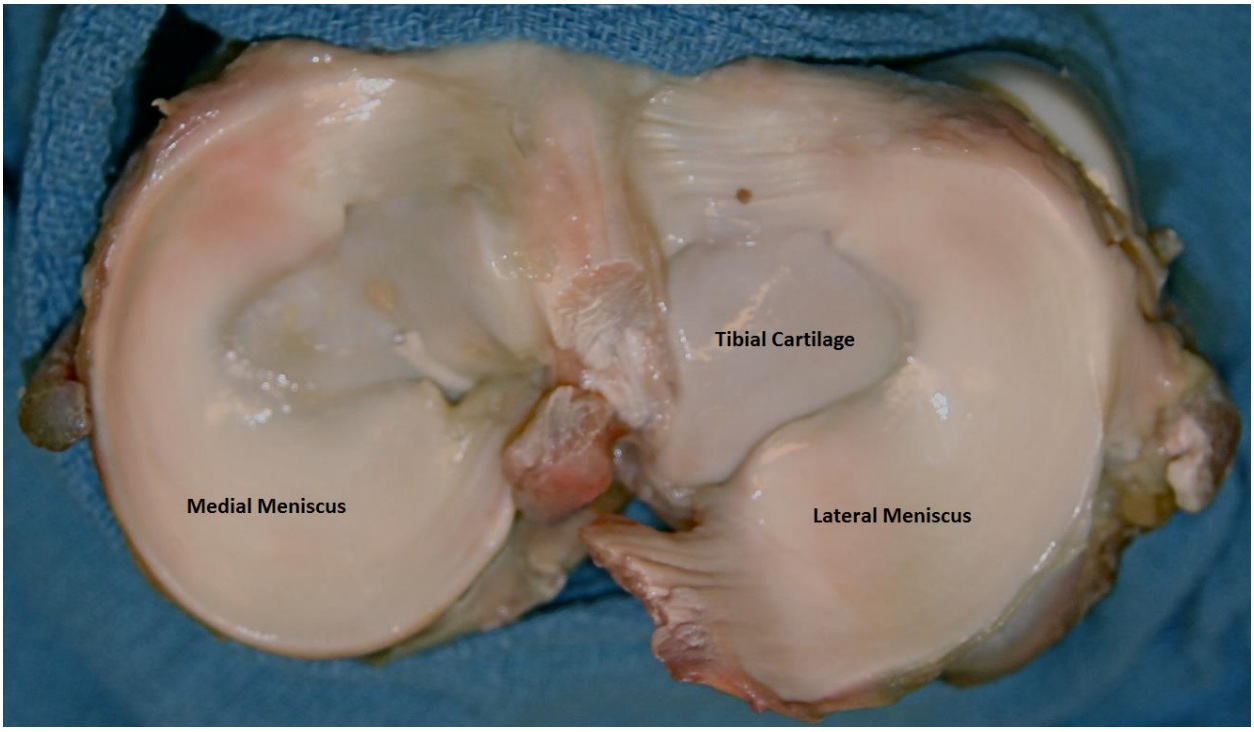

Figure 1.6 Dorsal view of each meniscus. Note that the cartilage and menisci look very similar outside of their geometry. This similarity is a result of being comprised of nearly identical components.

1.1.5. Ligaments

Ligaments connect bones together and are responsible for connecting the major components of the stifle, providing support and stability. The major stifle ligaments are:

- the medial and lateral collateral ligaments, which fasten the femur to the tibia on each side of the joint and provide support during flexion and extension
- the posterior and anterior cruciate ligaments (PCL and ACL), arranged like a letter "X" in the sagittal plane, connect the femur and tibia anteriorly/posteriorly. The PCL attaches to the posterior, proximal region of the tibia and connects to the anterior, distal portion of the femur. The ACL attaches to the anterior, proximal region of the tibia and connects to

the posterior, distal region of the femur. These ligaments are primarily responsible for constraining forward and backward slipping of the tibia.

- three patellar ligaments that extend from the quadriceps and insert into the tibia on the cranial side of the joint. These ligaments keep the patella in place and provide connection for the quadriceps to extend the joint. These ligaments also assist in total joint stability as they provide additional support to the femur to restrict forward translation. Additionally, the patellar ligaments give the stifle joint the unique ability to lock. This allows the horse to stand for many hours with minimal muscular effort.

The last major structure that comprises the stifle joint is the joint capsule. Most notably, the connective tissue that wraps around the trochlear ridge of the femur provides substantial joint support. As a whole, the stifle joint is incredibly tight with little wiggle room. This characteristic makes surgical access quite difficult.

1.1.6. Anatomical Similarity to Humans

The equine stifle joint is anatomically similar to humans both in structure and function. The horse stifle differs from the human knee in that it 1) lacks the ability to fully extend the joint (maximal equine extension is approximately 155°), 2) has more prominent intercondylar eminences, 3) a tighter connection between the tibia and femur resulting in reduced ease of surgical access, and 4) more patellar ligaments (three distinct ligaments versus ligament with two bundles).

Compared with other stifle joints, such as that in the canine, the equine stifle joint experiences closer loads to the human knee joint, is closer in size, and has similar thickness of articular cartilage, which is especially important when considering subchondral bone defects.

Because of the similarity between the two joints, humans experience many of the same injuries that horses do. This makes the equine stifle joint a robust animal model for translational research.

1.2. Subchondral Bone Lesions

1.2.1. Equine Bone Lesions

Equine subchondral bone is susceptible to cyst formation, particularly in growing horses, and the medial femoral condyle is the most common location. Research on equine subchondral bone cysts (SBCs), also referred to as subchondral cystic lesions (SCLs), began in 1968 with a study by Pettersson et al. that looked at radiolucent voids in the fetlock of the horse [1]. When sufficiently powerful portable radiograph machines were developed in the 1980's, SBCs were described in the stifle of the horse [2-5]. This early research was focused on describing the physical aspects of SBCs, most of which were large in size, causing lameness. This was (and still is) an unfortunate problem for most SBC cases presented to veterinarians. They present at a point at which the horse is already lame, as a result of a large, developed cyst [6]. This lack of early detection and diagnosis makes it rather difficult to accurately assess its true pathologenesis and progression mechanisms. Even still, veterinarian researchers have worked tirelessly to fit all of the pieces together. With the development of more efficient and higher detail digital radiography, and the increased scrutiny applied to growing racehorses, the last two decades have proven to be more fruitful than the previous two in understanding this crippling defect.

1.2.1.1. General Description

SBCs that occur in the stifle of the horse manifest themselves in different shapes and sizes, but the vast majority are located in the medial femoral condyle (MFC). In the late 1980's, White et al. described two types of SBCs: Type 1) a dome shaped cyst that was most commonly

coupled with a flattened femur, and Type 2) a circular cyst that articulated with the joint surface [7].

As radiographic technology improved, numerous SBC cases were presented to clinicians, and the diagnosis of SBCs evolved into more specific classifications. Since the field is still evolving, a universally accepted characterization scheme has not yet been established. However, most classification systems begin with a flattening of the femur and progress into a defect that is further characterized by its size. We have adopted the grading scheme of Santschi et al. [8] (Figure 1.7).

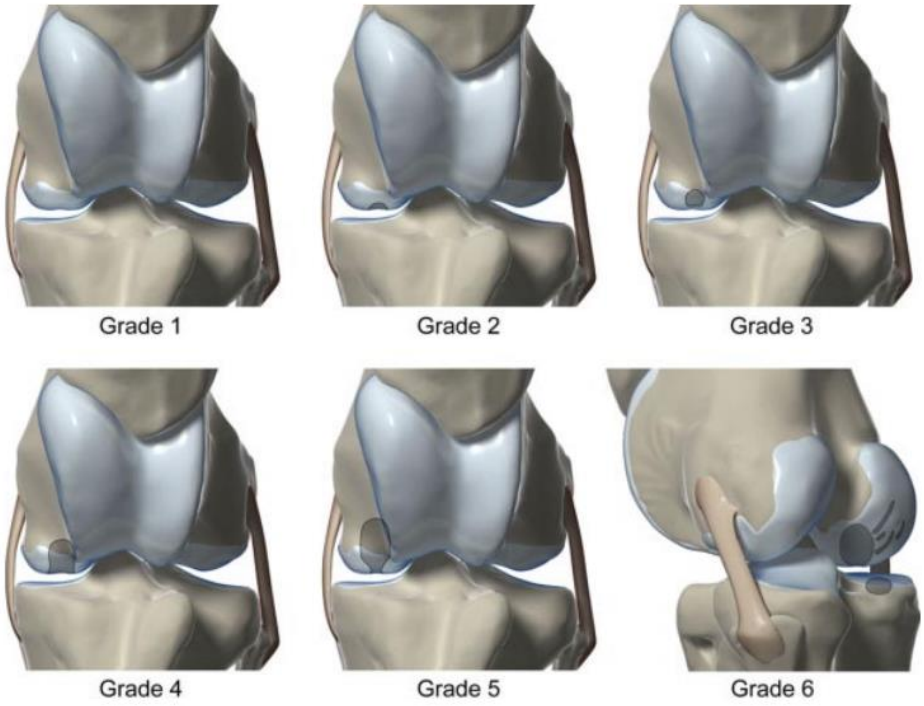

Figure 1.7 Classification of subchondral cystic lesions of the medial femoral condyle as described by Santschi et al. Grade 1 = flattening or a small defect in the subchondral bone of the central MFC, Grade 2 = a <10 mm height dome-shaped lucency, Grade 3 = a condylar lucency with no evidence of a cloaca in the subchondral bone, Grade 4 > 10 mm large dome shape

extending to the articular defect, Grade 5 > 10 mm lucency with a narrow cloaca at the articular surface, Grade 6 = a combination of Grade 4 or Grade 5 SCL and other lucencies in the caudal MFC or proximal medial tibial plateau. Reprinted from *The American College of Veterinary Surgeons*, 2014; 44:281-288 with permission.

1.2.1.2. Pathogenesis

The two most implicated "dominant" mechanisms for cyst development are trauma and osteochondrosis [4, 9]. Osteochondrosis is caused by failure of endochondral ossification due to a local interruption of blood supply to the growth cartilage. This causes retained areas of cartilage within developing bone which are susceptible to injury causing osteochondral clefts and fragmentation. It occurs in young humans and in rapidly growing animals, such as the horse. However, osteochondrosis does not explain the occurrence of SBCs in adult horses, the enlargement of SBC, or how researchers have been able to induce SBCs with cartilage or subchondral defects alone [10, 11]. One of the first studies claiming to experimentally create one of these SBCs was performed by Kold et al., when the team of researchers created a defect in the articular cartilage in the central weight-bearing portion of the medial femoral condyle of a horse [12]. However, such defects have not been reproduced by other clinicians investigating SBC formation after cartilage damage [6, 13]. Experimental osteochondral defects have produced SBCs, suggesting that bone damage is involved with their formation [13]. This lends further support to the notion that traumatic bone injury (single or multiple) is responsible for cyst development. Another hypothesis of cyst progression places emphasis on high fluid pressures within the cyst that are pushed in from the surrounding joint space [14]. Initially hypothesized to increase intra-osseous stress, a finite element analysis investigating pressurized fluid in a cyst demonstrated that pressurized fluid actually reduced stresses around the void, serving as a means

of stress-shielding. Though reduced stresses may cause an increase in bone resorption, they do not explain initial defect formation.

It is apparent from radiographs of lame horses afflicted with an SBC that the cysts develop in the bone in the weight bearing portion of the medial femoral condyle in extension (Figure 1.8). This is a helpful clue into the pathology, since it's known that this part of the femur experiences the highest stresses [15]. Trauma was considered a possible cause for these cystic lesions from their first description, and research began to critically examine the histological and clinical aspects of these cysts to uncover additional clues of its pathology [16].

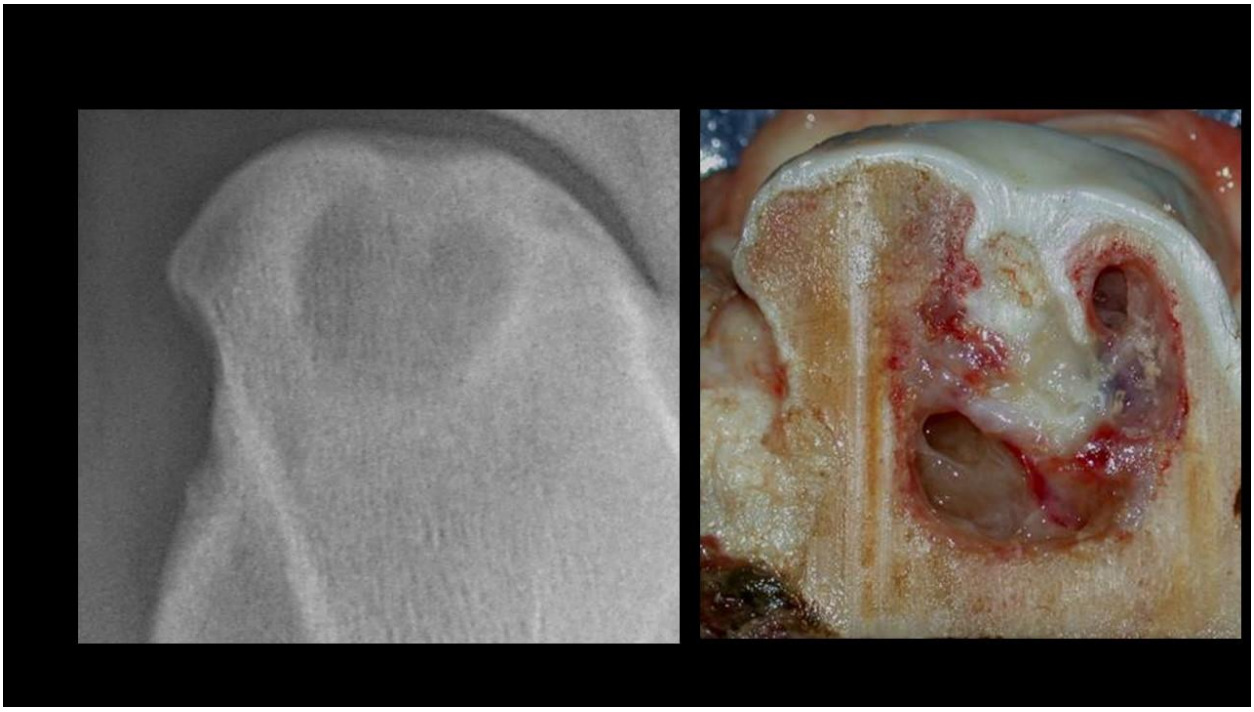

Figure 1.8 Visual comparison between a radiograph of a cystic lesion (left) and the gross anatomy of a cyst (right).

Histological examination of SBC contents reveals fibroplasia, capillary proliferation, fibrous tissue, as well as degenerated bone, cartilage, and disorganized areas of granulation tissue

and woven bone [7, 16]. The defect has a defined lining, a key characteristic in its nomenclature as a cyst, and is surrounded by sclerotic bone. There has also been work done in identifying the biological molecules involved with SBCs and what role they may play. Chemicals such as interleukin-6 and prostaglandin E3 are believed to be involved in an increase in bone resorption and slow-healing [17, 18]. These chemical factors may certainly have large influence on cyst progression.

With close examination of SBC contents and characteristics, more clues appear to support the mechanical trauma hypothesis.

- Sclerotic bone is generally a functional adaptation to over-loading of bone [19].
- The presence of cartilage suggests that the articular cartilage is collapsing (perhaps forcefully) into the void.
- Woven bone in non-fetal bones is typically created as part of a fracture healing response.
- Granulation tissue is present in healing wounds, suggesting the cyst is an externally influenced wound and not the result of an autoimmune disorder, or osteochondrosis without trauma.

However, the pathogenesis of SBCs has been (and still is) largely debated. In all likelihood, cyst development is a multifaceted phenomenon, and there will always be weaknesses in a hypothesis that tries to implicate a single mechanism. With that being said, it stands to reason that mechanics (perhaps even a single, forceful event of overload and the resulting bone damage and stresses) is the most influential in driving the cascade of events that lead to cyst initiation and development.

1.2.1.3. Treatment

Treatments for SBCs are focused on reducing local inflammation and promoting bone and cartilage healing. The first published work on treatment was by Kold et. al., as well as Stewart et al., when horses afflicted with a subchondral defect were given anti-inflammatory agents and assigned to periods of rest [2, 3]. While this method demonstrated some level of success, full radiographic recovery was rare, and older horses were not as responsive to the treatment.

When conservative treatments did not provide a high enough success rate for recovery, surgical treatments were resorted to in an attempt to expedite the recovery process. These surgical techniques tend to involve some variation of cyst debridement and refilling [20-22] (Figure 1.9). Arthroscopically, surgeons remove the articular cartilage at the distal aspect of the SBC and clean out the cyst. Once the cysts are debrided, the void is refilled with any combination of cancellous bone, bone substitutes, growth factors, chondrocyte grafts, mesenchymal stem cells, and fibrin glue [23, 24]. Treatment success rates range between 50% and 75%. However, there is little data about bone healing after debridement, and what data is available suggests that full radiographic healing occurs in less than 20% of patients [24]. Also, there is a scarcity of data examining the long-term resolution of lameness.

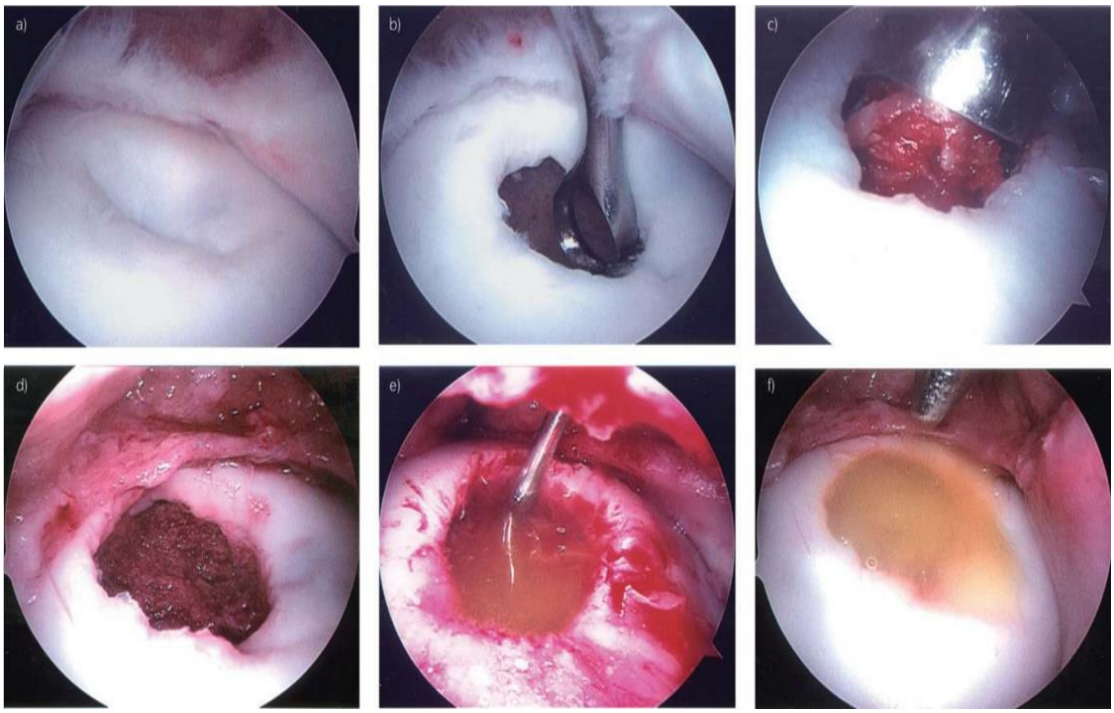

Figure 1.9 Surgical debridement and bone graft procedure [24]. Reprinted from the *Equine Veterinary Journal*, 2012; 44:606-613 with permission.

Recently, a treatment that places a screw in lag fashion across the defect has been reported to have a high rate of success [25]. This surgical procedure is the first of its kind, and seems to address the mechanics of SBC unlike any previous technique. A reasonable assumption is that the bone around the cyst is less able to carry the resulting increase in stresses. The stress concentration around the cyst is analogous to the classic "plate with a hole" analysis. This type of analysis shows increases in tension and shear stress around the hole. If such abnormal, elevated stresses are present, the bone healing around the cyst will be inhibited. The screw may help to reduce high bone stresses around the cyst to acceptable levels and provide an opportunity for the bone to heal. In fact, in a recent study using finite element analysis, McErlain et al. showed that Von Mises stresses were elevated in the bone immediately surrounding cysts [26]. However, there is still the possibility that fluid within the cyst is also providing a means of

stress-shielding, as mentioned earlier [14]. If this is the case, the screw placed in a lag fashion would then serve to restore stresses in the bone surrounding the cyst. In either case, it seems plausible that the lag screw somehow addresses the mechanical aspects of cyst development and healing, a paradigm shift in current treatment strategies.

1.2.2. Human Bone Lesions

Subchondral bone cysts are not unique to the equine population. In fact, humans (and other animals) also develop subchondral cystic lesions in their joints [27-30]. As is true with equine SBCs, the etiology and pathology of SBCs in humans is still debated, but many investigators/physicians have proposed possible causes. Perhaps the most dominant hypothesis in the field is that high, irregular stress transfer occurs between the femoral (or tibial) cartilage into the subchondral bone and mechanical trauma occurs. This theory is further supported by:

- Studies which have shown that high stresses in the subchondral bone can be a function of cartilage damage and irregularities [31].
- The clinical observation that SBCs are more common in osteoarthritic patients. In a study performed by Tanamas et al., it was found that in a sample population of 132 subjects with knee osteoarthritis, subchondral bone cysts were present in nearly 50% of them [32].

While the underlying cause of mechanical trauma is implicated in both humans and horses, it's the SBC in conjunction with osteoarthritis that differentiates the two, as equine SBCs commonly occur without osteoarthritis. This supports the bone trauma hypothesis. Because mechanical trauma is of great concern for both species, studies that investigate stresses

associated with SBCs are relevant for both species. Thus, the equine model presents several advantages for studying SBCs in humans [33]:

- Humans and horses have anatomically similar joints in which SBCs occur (see Anatomy).
- Studying SBCs in horses isolates SBCs from osteoarthritis, allowing research to focus on the cysts and neglect the confounding effects of osteoarthritis and the related inflammatory response.
- The mechanical loads experienced by both species when normalized to joint size are similar.

1.3. Application of Finite Element Modeling in Biomechanics

The finite element method (FEM) is a class of numerical techniques to approximate solutions of boundary value partial differential equations (PDEs). Finite element analysis (FEA) is the practical application of the FEM, most commonly used in structural mechanics. Developing a finite element model using commercially available software consists of four distinct steps: Geometry construction, discretizing the geometry into elements, assigning material properties to each element, and applying boundary conditions. In the first step, recent advances in software have allowed the usage of medical image data, such as Magnetic Resonance (MR) imaging or Computed Tomography (CT), as the canvas for segmentation. The segmentation process yields the geometric boundaries for discretization. This critical advance in software enables finite element models to have an anatomically accurate geometry. In the second step, the choice of elements primarily depends on the geometry used. The two traditional element types are tetrahedra or hexahedra. While hexahedral elements are preferred in most cases, preferred for

their computational efficiency and accuracy, they have difficulty in conforming to complex geometry, such as the curved cartilage on the medial femoral condyle. Tetrahedral elements are not as restricted in their ability to conform to a surface, making them a desirable element choice in anatomical models. Loads and boundary conditions imposed on the mesh nodes in step four create a displacement response. From these displacements, variables of interest, such as stress and strain, may be computed based on the material properties issued to each element in step three. However, this four step process assumes that commercially available software is available to set up the finite element equations and perform the legwork of calculation. In reality, the finite element method itself has its own unique step-by-step process, handled by the software of choice (ABAQUS) in this presented work. The process is as follows:

In the most general case of a static equilibrium finite element analysis, as is used in this thesis, we begin with an equilibrium statement (written in the classical form of the virtual work principle):

$$\int_{\Omega} \delta\epsilon^T \boldsymbol{\sigma} d\Omega = \int_{\Omega} \delta\mathbf{u}^T \mathbf{b} d\Omega + \int_{\Gamma} \delta\mathbf{u}^T \mathbf{t} d\Gamma$$

Here, **ε =** strains **σ** = the Cauchy stress matrix (internal stresses), δ = the Kronecker delta, **u** = displacements, **t** = external surface tractions, and **b** = external body forces. In the current analysis, body forces (i.e, gravity) are not present in the model, so the body force integral can be omitted. However, the integral containing the traction vector, **t**, represents external loading (i.e, a force applied to the proximal face of the femur) and is not omitted. The equation then reduces to:

$$\int_{\Omega} \delta\epsilon^T \boldsymbol{\sigma} d\Omega = \int_{\Gamma} \delta\mathbf{u}^T \mathbf{t} d\Gamma$$

We can then redefine the terms on each side of the equation based on standard continuum mechanics principles. Strains can be expressed as **B**·**a**, where **B** is a matrix containing differentials of defined shape functions (element dependent), and **a** is a vector containing the virtual nodal displacements. Stresses can be defined as **D**·**B**·**a**, where **D** is the elasticity matrix defined by:

$$D = \frac{E}{1-\nu^2}\begin{pmatrix} 1 & \nu & 0 \\ \nu & 1 & 0 \\ 0 & 0 & \frac{1-\nu}{2} \end{pmatrix}$$

Here, E and ν are material properties (elastic modulus and Poisson's ratio) that can be defined for each element (see chapters 2 and 3 for values used in this study). **u** is the overall element displacement that can be approximated by summing all nodal displacements, defined as **N**·**a**, where **N** is an interpolation function based upon the choice of element used in the discretization of the geometric domain. In this study, 4 node tetrahedral elements were chosen that have an interpolation function of:

$$\mathbf{N} = (1 - g - h - r)\,\mathbf{u_1} + g\,\mathbf{u_2} + h\,\mathbf{u_3} + r\,\mathbf{u_4}$$

where g, h, and r are parametric (unit) coordinate directions, and **u** are nodal displacements. Finally, we can rewrite the virtual work equation as:

$$\int_\Omega \delta\mathbf{a}\mathbf{B}^\mathsf{T}\mathbf{D}\mathbf{B}\mathbf{a}d\Omega = \int_\Gamma \delta\mathbf{a}\mathbf{N}^T\mathbf{t}d\Gamma$$

δ**a** can be removed from each side, which reduces the equation to:

$$\int_\Omega \mathbf{B}^\mathsf{T}\mathbf{D}\mathbf{B}d\Omega\mathbf{a} - \int_\Gamma \mathbf{N}^T\mathbf{t}d\Gamma = 0$$

Note this equation is applied at every element. Thus, the equations can be assembled globally to account for each element and written in matrix form as:

$$[K]\{a\} = \{f\}$$

by setting [K] equal to $\mathbf{B^T DB}$ and recognizing that the second integral represents a nodal force vector. This global set of nonlinear equations is then solved by an implicit solver in ABAQUS that utilizes the Newton method. Iterative steps also allow contact constraints, such as the penalty method (see chapter 2) or spring forces, to be applied as an additional surface force to specific nodes as the solution history progresses when appropriate. While this is the general process used by ABAQUS to formulate and solve the finite element equations, certain details of the ABAQUS solver are not addressed here in this introduction. For a more comprehensive review of the solver implemented in ABAQUS, see the ABAQUS theory manual.

It's difficult to track an exact origin to the finite element method, but it's often cited that the method was first developed by Courant in a 1942 address to the American Mathematical Society [34]. The aerospace field first adopted the method and it was quickly adapted into use by civil engineers in the 1950's [35]. By demonstrating near-perfect solutions, compared with analytical solutions, as well as experimental observation, FEA became an incredibly powerful tool, opening the door to a new breadth of research possibilities. As long as appropriate steps are taken to ensure the accuracy of the computational model (see *1.3.3. Verification* and *1.3.4. Validation*), there's little doubt in the validity of the results obtained through FEA.

1.3.1. Advantages of Finite Element Modeling

- Wide applicability
- Many different material properties can be incorporated, which is especially useful in a complex biological model with many different structures.
- Element size can be adaptively refined/coarsened to match any geometry.
- Commercial software is available to facilitate all necessary set-up, calculation, and post-processing
- Phenomena that would be otherwise impossible to examine with physical experiments can be analyzed.
- Nearly perfect solutions to problems with known analytical solutions have been demonstrated.
- Parameters can be quickly changed to perform a parametric study.

1.3.2. Disadvantages of Finite Element Modeling

- The solution is still an approximation.
- Assumptions are often made to simplify the problem, or to estimate an unknown quantity.
- Solutions are only calculated at mesh nodes.
- Validation can be difficult.

1.3.3. Verification

The American Society of Mechanical Engineers defines verification as, "the process of determining that a computational model accurately represents the underlying mathematical model and its solution" [36]. In other words, proper verification ensures that the equations are being solved correctly (remember that FEA is an approximation using numerical methods). A

large part of this process is verifying that the FEM algorithm, written as code, is accurate. A code can be verified by comparing its solution to a known analytical solution for a given problem. Most engineering researchers who use FEA implement it in commercially available software that has already been verified by the software developers. However, formulations are sometimes not clearly described, or disclosed (e.g, reduced integration), and the accuracy can be affected.

The other part of verification deals with the proper discretization of the domain. Since the finite element method provides solutions only at prescribed discrete locations, the solution of the rest of the domain is interpolated. Thus, enough degrees of freedom must be present in the model to accurately represent the solution for the entire domain. There should be negligible error from the interpolations. However, there's a delicate trade-off with discretization because the more degrees of freedom present in a model, the more expensive the computational cost. A trade-off then exists between efficiency and accuracy (Figure 1.10). One normally uses a model with the lowest number of degrees of freedom that provide an accurate solution. A mesh refinement convergence study is typically used to identify this model.

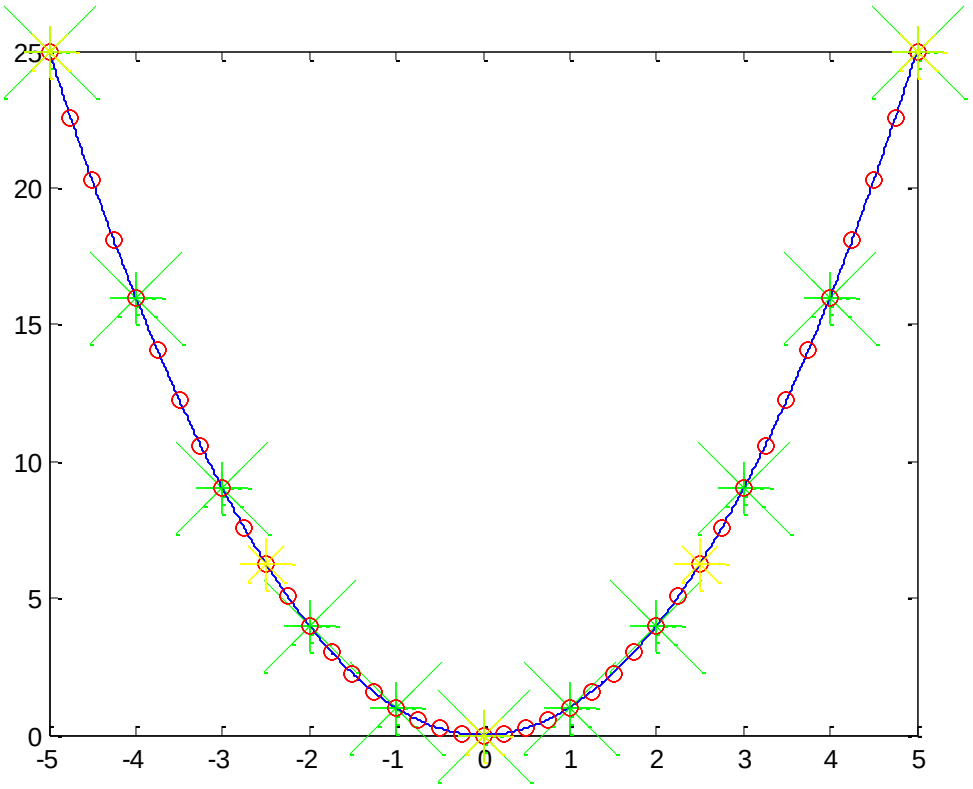

Figure 1.10 Representation of the trade-off between efficiency and accuracy. Consider a displacement solution that analytically looks like the curve through the dots. If nodes are prescribed at the yellow locations, the curvature of the solution will not be realized. However, if nodes are prescribed at the red locations, many redundancies are present, costing much more computational time to converge on a solution. Alternatively, if nodes are prescribed at the green locations, the accuracy of the red discretization is maintained, yet at a fraction of the computational cost.

As mentioned earlier, the proper way to deal with the accuracy/efficiency trade-off is to perform a convergence analysis. A convergence analysis will help to determine the minimum number of nodes needed to produce a result similar to that of a hypothetical infinite number of nodes. Beginning with a very coarse mesh, the model is analyzed to determine the desired output

variable(s) (maximum principal stress accurately, for example). The mesh is then refined by a reasonable increment (making the new element size approximately half of the previous element is common, although smaller increments may be used). The comparison output variable is again generated, and the results are compared with the previous iteration. If a <5% difference occurs in the two solutions, the mesh for the previous iteration is accepted [37]. If not, the mesh is refined again, and the comparison is repeated.

1.3.4. Validation

Validation is defined as, "the process of determining the degree to which a model is an accurate representation of the real world from the perspective of the intended uses of the model" [36]. In other words, are the right equations being solved? Do the physics of the system represent reality? Validation is perhaps the most difficult part of computational modeling, as there is no definitive way to guarantee the answers to these two questions are with 100% certainty. However, as Henninger et al. state:

> *The "truth" about the system is a statistically meaningful prediction that can be made for a specific set of boundary conditions [38]*.

Therefore, the goal is not to model *in vivo* reality with absolute certainty, but to take necessary actions that develop a statistically meaningful result.

The typical approach in validation of a model is to perform physical experiments that determine a meaningful variable in a system and compare that with the model's output. Depending on the research goal, validation may take a number of forms. For example, a direct form of validation would be to experimentally test the material properties of each structure represented in the model and then determine a governing equation for the given behavior. These

equations would then be introduced into the model for each structure present. The next step would be performing an experiment, for example, looking at tibial contact pressure with 500 Newtons of compressive force applied to the proximal femur (assuming a knee model is being developed). Then, the same task would be performed with the computational model, and the contact pressures would be compared. If the two are in accord, there is now concrete validity in the model's physical behavior for that specific task. Remember, models are typically developed for a very specific research goal. Unfortunately, this direct form of validation is not always feasible. In many preliminary or investigational studies material properties are not explicitly determined, and one must find appropriate material properties and boundary conditions based on what is available in the literature. Different experiments in the literature may yield different material properties for the same biological structure which is a consequence of different testing procedures or specimen-to-specimen differences. If this is the case, a sensitivity analysis is performed. A sensitivity analysis is the process of using a wide range of available material properties, say for cartilage, and investigating the impact it has on the output parameter such as contact pressure on the tibial plateau. If the result does not change with varying that property, the model is not sensitive to that property. Thus, any reasonable value available is justified. If the output changes significantly with varying properties, then the behavior may be bounded by using the max/min property values and/or the property value can be judiciously chosen based on the model application (like instantaneous or relaxation modulus).

One of the problems with validation is that experimental methods also have a level of uncertainty. If indirect validation is all that the researcher has available, they compare their model's kinetic and/or kinematic results to what other validated models and/or related experiments have demonstrated.

1.3.5. Biomechanics

It was no surprise that two decades after its initial development, finite element analysis was integrated into biomechanics research, a field replete with unanswered questions. Its popularity snowballed, with more and more researchers understanding that FEA provided a means of performing biological research that would otherwise be difficult, or even impossible, to do experimentally. Because of this, just as it did in the civil engineering discipline, FEA opened the door to countless research opportunities. In particular, the medical community has reaped invaluable rewards from the application of FEA to biomechanics, such as the development of safer, more efficient stents, more robust orthopedic implants, a deeper insight into some of our body's mechanics, and the consequences when these mechanics become compromised [28, 39-45].

Since its adaptation into biomechanics, a rapid increase in computational power and improved modeling techniques have paved the way for more complex finite element models. Led by landmark studies [44, 46-50], the road eventually led to accurate models of complex joints, such as the knee (or stifle). Representing the kinetics and kinematics with high fidelity is no easy task, considering just how complex the knee really is. Yet, researchers have shown time and time again that it is possible [40-44, 48, 50-53]. For example, Mootanah et al. developed a computational knee model to evaluate the efficacy of surgical treatments of osteoarthritis [43]. They were able to successfully compare the kinematic data of their model to an *in vitro* result. Halloran et al. created a knee model that investigated the mechanics of total knee replacements. They were able to match the kinematic data of their model with data taken experimentally from a knee simulator [40]. The advances made in computational modeling have been nothing short of monumental. Now, practically anyone with a foundational understanding of FEA and a

knowledge of their biomechanical application can stand on the shoulders of giants and create a robust, validated model tailored to their research needs.

1.4. Putting It All Together

Literature regarding equine bone cysts reveals an interesting trend; research has been largely devoted to possible treatments and treatment efficacy. It seems a gap has developed between pathological understanding and treatment strategies, most likely a result of the difficulty in examining subchondral defects in a living horse. A problem concerning intra-osseous stresses would be difficult, if not impossible, to examine with experimental technologies available. Finite element analysis provides the essential research tool needed to help fill this gap that has developed. This work will be the first of its kind to use equine medical image data, construct a finite element model, and analyze the stresses of the medial femoral condyle with and without subchondral defects.

Ultimately, both the equine and human communities want the same thing: the full understanding of subchondral bone cysts and the best way to treat them with available technologies. David Hume famously said that truth is made known through argument amongst friends. Research from the last five decades put us closer than ever to the truth regarding the pathogenesis of SCLs (SBCs). Researchers from across the world continue to publish hypothesis-driven research, uncovering more and more clues behind this mystery. Discovering the mechanical consequences of subchondral bone cysts will be another step toward understanding this disease and finding a reliable treatment.

1.5. References

[1] Pettersson, H., and Sevelius, F., 1968, "Subchondral Bone Cysts in the Horse: A Clinical Study," Equine Veterinary Journal, 1(2), pp. 75-82.

[2] Stewart, B., and Reid, C. F., 1982, "Osseous Cyst-Like Lesions of the Medial Femoral Condyle in the Horse," J Am Vet Med Assoc, 180(3), pp. 254-7.

[3] Jeffcott, L. B., and Kold, S. E., 1982, "Clinical and Radiological Aspects of Stifle Bone Cysts in the Horse," Equine Veterinary Journal, 14(1), pp. 40-46.

[4] Mcilwraith, C. W., 1982, "Subchondral Cystic Lesions (Osteochondrosis) in the Horse," Compend Contin Educ Pract Vet, 4(pp. s282-s294.

[5] Baxter, G., 1996,

[6] Mcilwraith, C., 2015,

[7] White, N. A., Mcilwraith, C. W., and Allen, D., 1988, "Curettage of Subchondral Bone Cysts in Medial Femoral Condyles of the Horse," Equine Veterinary Journal, 20(pp. 120-124.

[8] Santschi, E. M., Williams, J. M., Morgan, J. W., Johnson, C. R., Bertone, A. L., and Juzwiak, J. S., 2015, "Preliminary Investigation of the Treatment of Equine Medial Femoral Condylar Subchondral Cystic Lesions with a Transcondylar Screw," Vet Surg, 44(3), pp. 281-8.

[9] "Ray Cs, Mcilwraith Cw - 1996 - Development of Subchondral Cystic Lesions after Articular Cartilage and Subchondral Bone Damage,"

[10] Yovich, J. V., and Stashak, T. S., 1989, "Subchondral Osseous Cyst Formation after an Intra-Articular Fracture in a Filly," Equine Veterinary Journal, 21(1), pp. 72-74.

[11] Mcilwraith, C., 1993, "What Is Developmental Orthopedic Disease, Osteochondrosis, Osteochondritis, Metabolic Bone Disease?," Am Assoc Equine Pract, 39(pp. 35-44.

[12] Kold, S. E., Hickman, J., and Melsen, F., 1986, "An Experimental Study of the Healing Process of Equine Chondral and Osteochondral Defects," Equine Vet J, 18(1), pp. 18-24.

[13] Ray, C. S., Baxter, G. M., Mcilwraith, C. W., Trotter, G. W., Powers, B. E., Park, R. D., and Steyn, P. F., 1996, "Development of Subchondral Cystic Lesions after Articular Cartilage and Subchondral Bone Damage in Young Horses," Equine Veterinary Journal, 28(3), pp. 225-232.

[14] Cox, L. G., Lagemaat, M. W., Van Donkelaar, C. C., Van Rietbergen, B., Reilingh, M. L., Blankevoort, L., Van Dijk, C. N., and Ito, K., 2011, "The Role of Pressurized Fluid in Subchondral Bone Cyst Growth," Bone, 49(4), pp. 762-8.

[15] Maquet, P., Van De Berg, A., and Simonet, J., 1975, "Femorotibial Weight-Bearing Areas. Experimental Determination," The Journal of Bone & Joint Surgery, 57(6), pp. 766-771.

[16] Jeffcott, L. B., Kold, S. E., and Melsen, F., 1983, "Aspects of the Pathology of Stifle Bone Cysts in the Horse," Equine Vet J, 15(4), pp. 304-11.

[17] Svon Rechenberg, B., Leutenegger, C., Zlinsky, K., Mcilwraith, C. W., Akens, M. K., and Auer, J. A., 2001, "Upregulation of Mrna of Interleukin-1 and -6 in Subchondral Cystic Lesions of Four Horses," Equine Veterinary Journal, 33(2), pp. 143-149.

[18] Von Rechenberg, B., Guenther, H., Mcilwraith, C. W., Leutenegger, C., Frisbie, D. D., Akens, M. K., and Auer, J. A., 2000, "Fibrous Tissue of Subchondral Cystic Lesions in Horses Produce Local Mediators and Neutral Metalloproteinases and Cause Bone Resorption in Vitro," Vet Surg, 29(5), pp. 420-9.

[19] Day, J. S., Van Der Linden, J. C., Bank, R. A., Ding, M., Hvid, I., Sumner, D. R., and Weinans, H., 2004, "Adaptation of Subchondral Bone in Osteoarthritis," Biorheology, 41(3-4), pp. 359-68.

[20] Lewis, R., 1987,

[21] Howard, R. D., Mcilwraith, C. W., and Trotter, G. W., 1995, "Arthroscopic Surgery for Subchondral Cystic Lesions of the Medial Femoral Condyle in Horses: 41 Cases (1988-1991)," J Am Vet Med Assoc, 206(6), pp. 842-50.

[22] Smith, M. A., Walmsley, J. P., Phillips, T. J., Pinchbeck, G. L., Booth, T. M., Greet, T. R., Richardson, D. W., Ross, M. W., Schramme, M. C., Singer, E. R., Smith, R. K., and Clegg, P. D., 2005, "Effect of Age at Presentation on Outcome Following Arthroscopic Debridement of Subchondral Cystic Lesions of the Medial Femoral Condyle: 85 Horses (1993--2003)," Equine Vet J, 37(2), pp. 175-80.

[23] Bodo, G., Hangody, L., Modis, L., and Hurtig, M., 2004, "Autologous Osteochondral Grafting (Mosaic Arthroplasty) for Treatment of Subchondral Cystic Lesions in the Equine Stifle and Fetlock Joints," Vet Surg, 33(6), pp. 588-96.

[24] Ortved, K. F., Nixon, A. J., Mohammed, H. O., and Fortier, L. A., 2012, "Treatment of Subchondral Cystic Lesions of the Medial Femoral Condyle of Mature Horses with Growth Factor Enhanced Chondrocyte Grafts: A Retrospective Study of 49 Cases," Equine Vet J, 44(5), pp. 606-13.

[25] Santschi, E. M., Williams, J. M., Morgan, J. W., Johnson, C. R., Bertone, A. L., and Juzwiak, J. S., 2015, "Preliminary Investigation of the Treatment of Equine Medial Femoral Condylar Subchondral Cystic Lesions with a Transcondylar Screw," Vet Surg, 44(3), pp. 281-8.

[26] Mcerlain, D. D., Milner, J. S., Ivanov, T. G., Jencikova-Celerin, L., Pollmann, S. I., and Holdsworth, D. W., 2011, "Subchondral Cysts Create Increased Intra-Osseous Stress in Early Knee Oa: A Finite Element Analysis Using Simulated Lesions," Bone, 48(3), pp. 639-46.

[27] Audrey, H. X., Abd Razak, H. R., and Andrew, T. H., 2014, "The Truth Behind Subchondral Cysts in Osteoarthritis of the Knee," Open Orthop J, 8(pp. 7-10.

[28] Durr, H. D., Martin, H., Pellengahr, C., Schlemmer, M., Maier, M., and Jansson, V., 2004, "The Cause of Subchondral Bone Cysts in Osteoarthrosis: A Finite Element Analysis," Acta Orthop Scand, 75(5), pp. 554-8.

[29] Guermazi, A., Hayashi, D., Roemer, F. W., Niu, J., Yang, M., Lynch, J. A., Torner, J. C., Lewis, C. E., Sack, B., Felson, D. T., and Nevitt, M. C., 2010, "Cyst-Like Lesions of the Knee Joint and Their Relation to Incident Knee Pain and Development of Radiographic Osteoarthritis: The Most Study," Osteoarthritis Cartilage, 18(11), pp. 1386-92.

[30] Kaspiris, A., Khaldi, L., Grivas, T. B., Vasiliadis, E., Kouvaras, I., Dagkas, S., Chronopoulos, E., and Papadimitriou, E., 2013, "Subchondral Cyst Development and Mmp-1 Expression During Progression of Osteoarthritis: An Immunohistochemical Study," Orthop Traumatol Surg Res, 99(5), pp. 523-9.

[31] Pallante-Kichura, A. L., Cory, E., Bugbee, W. D., and Sah, R. L., 2013, "Bone Cysts after Osteochondral Allograft Repair of Cartilage Defects in Goats Suggest Abnormal Interaction between Subchondral Bone and Overlying Synovial Joint Tissues," Bone, 57(1), pp. 259-68.

[32] Tanamas, S. K., Wluka, A. E., Pelletier, J.-P., Martel-Pelletier, J., Abram, F., Wang, Y., and Cicuttini, F. M., 2010, "The Association between Subchondral Bone Cysts and Tibial Cartilage Volume and Risk of Joint Replacement in People with Knee Osteoarthritis: A Longitudinal Study," Arthritis Research & Therapy, 12(2), pp. R58-R58.

[33] Gregory, M. H., Capito, N., Kuroki, K., Stoker, A. M., Cook, J. L., and Sherman, S. L., 2012, "A Review of Translational Animal Models for Knee Osteoarthritis," Arthritis, 2012(pp. 764621.

[34] Courant, R., 1943, "Variational Method for the Solution of Problems of Equilibrium and Vibrations," Am. Math Soc, 49), pp. 1-43.

[35] Martin, H., 1966, "Introduction to Matrix Methods of Structural Analysis," McGraw-Hill, pp.

[36] Engineers, A. S. O. M., 2006,

[37] Jones, A. C., and Wilcox, R. K., 2008, "Finite Element Analysis of the Spine: Towards a Framework of Verification, Validation and Sensitivity Analysis," Medical Engineering & Physics, 30(10), pp. 1287-1304.

[38] Henninger, H. B., Reese, S. P., Anderson, A. E., and Weiss, J. A., 2010, "Validation of Computational Models in Biomechanics," Proc Inst Mech Eng H, 224(7), pp. 801-12.

[39] Davids, N., and Mani, M. K., 1972, "Effects of Turbulence on Blood Flow Explored by Finite Element Analysis," Computers in Biology and Medicine, 2(4), pp. 311-319.

[40] Halloran, J. P., Petrella, A. J., and Rullkoetter, P. J., 2005, "Explicit Finite Element Modeling of Total Knee Replacement Mechanics," Journal of Biomechanics, 38(2), pp. 323-331.

[41] Hull, M. L., 2002, "A Finite Element Model of the Human Knee Joint for the Study of Tibio-Femoral Contact," Journal of Biomechanical Engineering, 124(3), pp. 273.

[42] Kiapour, A., Kiapour, A. M., Kaul, V., Quatman, C. E., Wordeman, S. C., Hewett, T. E., Demetropoulos, C. K., and Goel, V. K., 2014, "Finite Element Model of the Knee for Investigation of Injury Mechanisms: Development and Validation," J Biomech Eng, 136(1), pp. 011002.

[43] Mootanah, R., Imhauser, C. W., Reisse, F., Carpanen, D., Walker, R. W., Koff, M. F., Lenhoff, M. W., Rozbruch, S. R., Fragomen, A. T., Dewan, Z., Kirane, Y. M., Cheah, K., Dowell, J. K., and Hillstrom, H. J., 2014, "Development and Validation of a Computational Model of the Knee Joint for the Evaluation of Surgical Treatments for Osteoarthritis," Comput Methods Biomech Biomed Engin, 17(13), pp. 1502-17.

[44] Peña, E., Martínez, M. A., Calvo, B., Palanca, D., and Doblaré, M., 2005, "A Finite Element Simulation of the Effect of Graft Stiffness and Graft Tensioning in Acl Reconstruction," Clinical Biomechanics, 20(6), pp. 636-644.

[45] Seshadhri, S., Janiga, G., Beuing, O., Skalej, M., and Thévenin, D., 2011, "Impact of Stents and Flow Diverters on Hemodynamics in Idealized Aneurysm Models," Journal of Biomechanical Engineering, 133(7), pp. 071005-071005.

[46] Bartel, D. L., Bicknell, V. L., and Wright, T. M., 1986, "The Effect of Conformity, Thickness, and Material on Stresses in Ultra-High Molecular Weight Components for Total Joint Replacement," J Bone Joint Surg Am, 68(7), pp. 1041-51.

[47] Berend, M. E., Ritter, M. A., Meding, J. B., Faris, P. M., Keating, E. M., Redelman, R., Faris, G. W., and Davis, K. E., 2004, "Tibial Component Failure Mechanisms in Total Knee Arthroplasty," Clin Orthop Relat Res, 428), pp. 26-34.

[48] Donahue, T. L. H., Hull, M. L., Rashid, M. M., and Jacobs, C. R., 2003, "How the Stiffness of Meniscal Attachments and Meniscal Material Properties Affect Tibio-Femoral Contact Pressure Computed Using a Validated Finite Element Model of the Human Knee Joint," J Biomech, 36(1), pp. 19-34.

[49] Godest, A. C., Beaugonin, M., Haug, E., Taylor, M., and Gregson, P. J., 2002, "Simulation of a Knee Joint Replacement During a Gait Cycle Using Explicit Finite Element Analysis," J Biomech, 35(2), pp. 267-75.

[50] Pena, E., Calvo, B., Martinez, M. A., and Doblare, M., 2006, "A Three-Dimensional Finite Element Analysis of the Combined Behavior of Ligaments and Menisci in the Healthy Human Knee Joint," J Biomech, 39(9), pp. 1686-701.

[51] Dhaher, Y. Y., Kwon, T. H., and Barry, M., 2010, "The Effect of Connective Tissue Material Uncertainties on Knee Joint Mechanics under Isolated Loading Conditions," J Biomech, 43(16), pp. 3118-25.

[52] Kazemi, M., Dabiri, Y., and Li, L. P., 2013, "Recent Advances in Computational Mechanics of the Human Knee Joint," Comput Math Methods Med, 2013(pp. 718423.

[53] Papaioannou, G., Demetropoulos, C. K., and King, Y. H., 2010, "Predicting the Effects of Knee Focal Articular Surface Injury with a Patient-Specific Finite Element Model," The Knee, 17(1), pp. 61-68.

2. Effects of Mesh Refinement, Meniscal Attachment, and Material Properties on the Accuracy of a Model of the Equine Stifle Joint

2.1. Abstract

In this paper, several finite element models of an equine stifle joint are compared to determine the most appropriate model for investigating bone cysts in future work, as well as to understand the effects of meniscal attachment complexity and material property changes on the accuracy of the model. We found that the complexity in the meniscal attachment is critical when evaluating maximum principal stresses in the bone. We also demonstrate that convergence for one output variable does not assure convergence for other output variables. Lastly, we illustrate that simplified material properties can be justified when the relationship between each material property and the desired output variables is understood.

Keywords: knee; meniscus; numerical convergence; contact model; stifle

2.2. Introduction

In the rapidly-growing field of computational biomechanics, it can become easy to overlook the basic essentials that give this tool real-world validity [1]. With the desire of obtaining information about biological systems and tissues that would otherwise be difficult or impossible to experimentally test, the level of complexity of each problem is generally high, and thus, subject to various errors and pitfalls. Therefore, it is the investigator's responsibility to verify and validate their model in order to convince themselves and their peers that the results have real-world meaning.

One of the most critical advancements in the field of computational mechanics was the adoption of finite element analysis into the field of engineering in the 1950's, although the original invention of the finite element method was presented in a 1942 address to the American Mathematical Society [2, 3]. However, it wasn't until the 1970's when finite element analysis was applied to and became the mainstay in computational biomechanics [4-6]. Since then, countless studies have used this method to investigate biological systems and reveal findings that may be nearly impossible to acquire experimentally.

With a rapid increase in computational power, the complexity of these finite element models has also increased over the past 40 years. In particular, models of the knee joint have become ubiquitous in the field [7-9]. With a wealth of literature investigating different material properties, boundary conditions, and behavior of the joint, researchers have an abundance of examples of how to (and not to) validate their model. Unfortunately, many neglect the verification process in computational modeling, most specifically sensitivity and convergence analyses. Weiss et al. succinctly describes these analyses and their importance in computational biomechanics [1]. When considering computational knee models, the verification process is perhaps more important as it is one of the body's most complex joints [10].

Material properties and boundary condition parameters derived experimentally are subject to error, especially since biological tissues are not identical within or across species [11]. Specimen-to-specimen error, as well as differences in experimental testing protocol can manifest itself in the model, whether recognized or not [12]. Without properly addressing each source of error, the statistical and clinical relevance of the results will consequently be compromised.

Our lab is currently investigating bone cysts that develop in young, racing horses. Medial femoral condyle (MFC) subchondral bone cysts (SBC) develop in the trabecular and subchondral

bone of the MFC of young horses, and can cause lameness and limit performance [13]. Current treatments result in mediocre success (~66%), are expensive, require long healing times, and have poor radiographic improvement. Recent clinical evidence in the horse indicates that lag screw placement across the MFC (ideally aimed through the SBC) promotes bone healing and lameness resolution [14], but little is known about the biomechanics of an intact or damaged MFC, or how the mechanics can be used to optimize healing. In future studies, we aim to develop a finite element model to investigate the mechanics behind cyst growth and the effects of an implanted screw.

In this paper, a controlled verification study on an equine stifle (knee) joint model is performed for two reasons: 1) determine the most appropriate model for our current applications, as well as 2) to investigate and discuss a few pertinent findings in the general context of the verification process.

2.3. Methods

2.3.1. Model Development

This study involved the development of multiple knee models in light of different published approaches. First, a convergence analysis was performed and comparisons were made by looking at different output parameters (Tables 2.4-2.6). Secondly, comparisons were made between relative complexities of the model, focused mainly on the meniscal properties, meniscal attachment to and interaction with the tibial plateau, and how these parameters affects the results (Table 2.1). Lastly, comparisons were made between specific material properties (cartilage, meniscus, and bone property changes) and how these properties affected the desired output parameter (e.g, bone stresses, or cartilage stresses) (Table 2.8).

CT data of an equine stifle joint was obtained from a young Thoroughbred and imported into ScanIP v7.0 (Simpleware, United Kingdom) (247x247x130 voxels, 0.7, 0.7, 1.0 mm spacing). The 3D geometry was generated by semi-automatically segmenting joint structures, under the supervision of a Professor of Veterinary Surgery. An example of this segmentation to mesh transition is demonstrated in Figure 2.1. The joint geometry was subsequently converted into solid, four-node tetrahedral elements (C3D4) using FE Free (Simpleware) to create the finite element mesh. The mesh was then imported into the ABAQUS FE package v6.14 (Dassault Systems, France) for finite element analysis.

Five distinct models were created to form the basis of this study (Merged, Tied, Tied with Anisotropy, Springs, Springs with Anisotropy), which are individually described below. To create each model used in this study, four separate mesh sections constituting the stifle joint were generated (Simpleware) and assembled/completed in ABAQUS (Figures 2.1-2.3). A spherical region of interest was created at the articulating surface of the femur for data extraction (Figure 2.2).

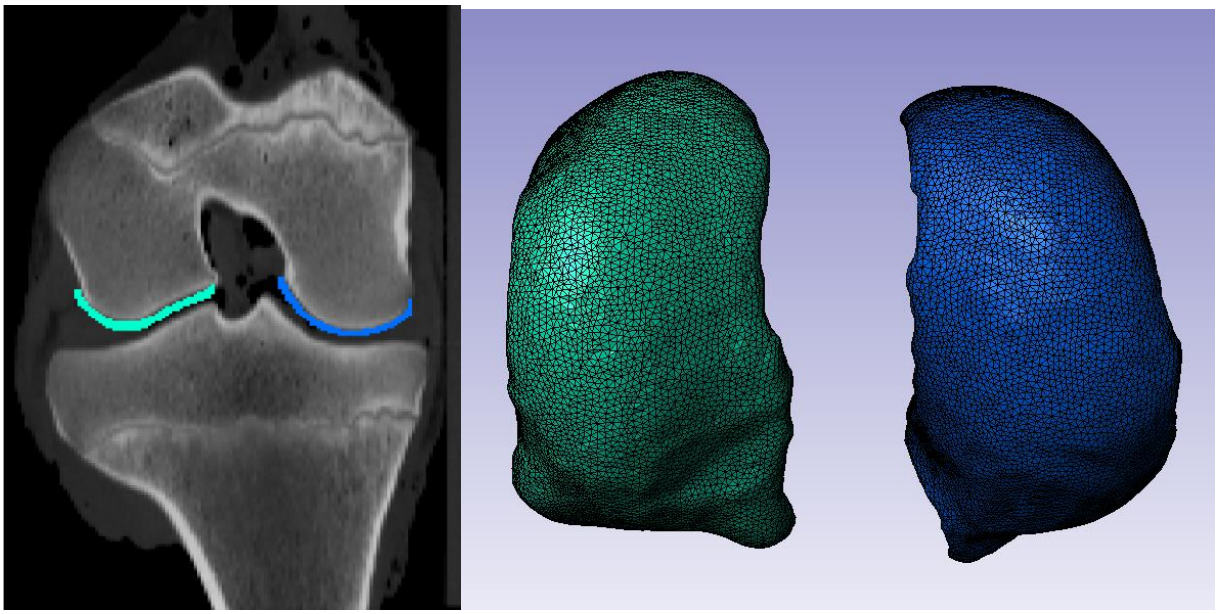

Figure 2.1 Coronal slice of the manually segmented masks for both the lateral and medial femoral cartilages (left). The full femoral cartilage meshes (right) having passed through the meshing algorithm (Simpleware).

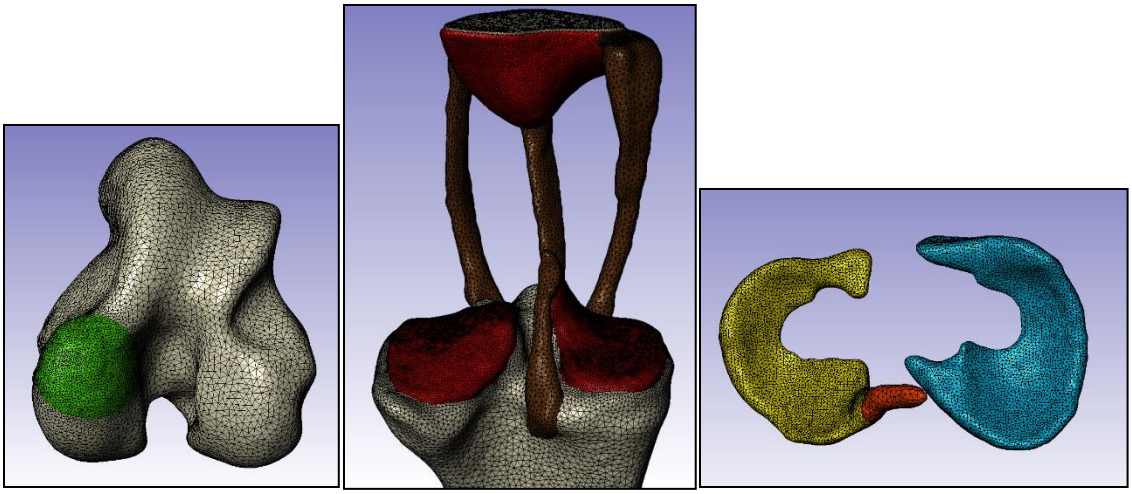

Figure 2.2 Mesh images generated in Simpleware, from left to right: (1) The femoral bone mesh consisting of the femoral bone (gray) and (2) the femoral bone region of interest (ROI) (green), (3) The tibia/patella mesh consisting of the tibia (grey), tibial and patellar cartialges (red), and the patellar/posteroir cruciate ligaments (brown). The PCL was included as a natural constraint, and the ACL was omitted, as it would not be loaded under the BC's used in this study. (4) The meniscal mesh consisting of the medial (blue) and lateral (yellow) meniscus, as well as the lateral meniscal/femoral ligament (orange).

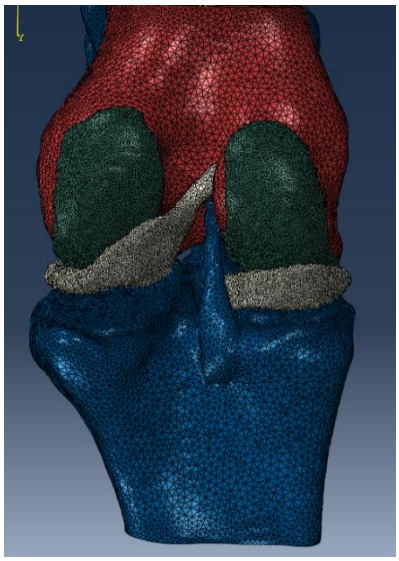

Figure 2.3 Posterior view of all four mesh sections (shown in different colors) assembled in ABAQUS into a complete model.

Separate meshes were generated in order to preserve mesh quality (dihedral angle $10<\Theta<160$ for each element) for each anatomical structure. When small gaps are present between segmented masks, the meshing algorithm attempts to preserve these gaps, however the smoothness and element quality are compromised in this process (Figure 2.4). To avoid poor mesh surface quality (dihedral angles outside of the acceptable range or visible surface roughness), we separated and grouped structures with continuous boundaries and meshed them separately.

Figure 2.4 Axial slice of the segmentation process with all knee structures shown. Voxel gaps, or holes between contacting surfaces, have been circled in black. In vivo, these gaps would most likely be filled with synovial fluid, however synovial fluid was not directly modeled in this study.

To determine what material properties and boundary conditions/tissue interactions to use for each soft tissue/model, the literature was reviewed, and appropriate values were determined. However, to implement the bone properties, a unique bone mapping feature within ScanIP was used to create a spectrum of properties based on Hounsfield units.

Hounsfield units were related to mass density using Equation 1. The mass density was then related to Young's Modulus using Equation 2.

$$\text{Mass Density} = (1.067*10^{-3})*\text{GrayScale} \quad (1)$$

$$\text{Young's Modulus} = (6.0*10^{3})*\text{MassDensity}^{2.5} \quad (2)$$

The power of 2.5 for the modulus equation accounted for the wide range of bone densities, where $E \alpha \rho^3$ for high density bone and $E \alpha \rho^2$ for low density bone. This resulted in Young's Modulus ranging from 50 MPa to 21,000 MPa.

2.3.1.1. Merged Model

To create the Merged model, the meniscus was combined with the tibial cartilage in the pre-processor (Simpleware) prior to meshing and given a single material property (Figure 2.5). Thus, the nodes between the meniscus and tibial cartilage are shared, and no other constraint was between these two structures was implemented in ABAQUS. The Merged model is the only model that has shared nodes between the two structures, and all other models used a separate meniscus mesh with manually created constraints in ABAQUS.

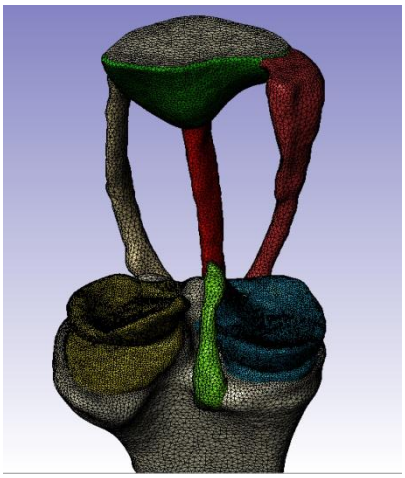

Figure 2.5 Tibia/patella mesh used for the merged model, which combines meshes 2 and 3 from Figure 2.2

2.3.1.2. Tied Model

The Tied model was made by manually creating tie constraints between the inferior meniscal face and the superior tibial cartilage (Figure 2.6).

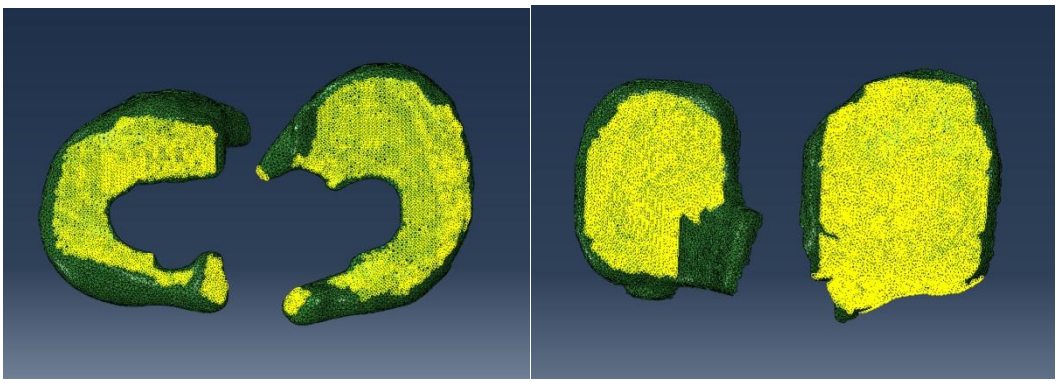

Figure 2.6 Tie constraints (yellow) between the menisci (left) and the tibial cartilage (right). Note that the tie constraints of the meniscal horns are also shown. Although the tibial cartilage tie surface extends beyond the meniscal surface, ABAQUS ignores tie constraints beyond a set tolerance distance, consequently making the prescription of tied surfaces easier.

2.3.1.3. Tied Anisotropy Model

The Tied Anisotropy model was identical to the Tied model, except anisotropic properties (Table 2.2) were used for the meniscus.

2.3.1.4. Springs Model

The Springs model introduced the allowance of meniscal translation on the tibia that is restrained by using springs (Table 2.2) to model the meniscal/tibial cartilage relationship (Figure 2.7). This arrangement is often used to account for capsular attachments/restriction on the meniscus.

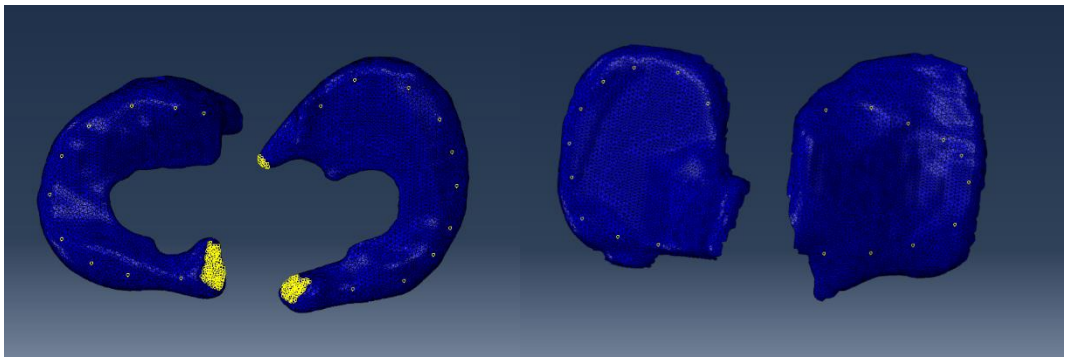

Figure 2.7 Spring interactions between meniscus and tibial cartilage implemented in ABAQUS. Spring attachments are shown in yellow with the menisci on the left and the tibial cartilage on the right. Note that the tie constraints of the meniscal horns are also shown in yellow. The springs apply a force constraint governed by Hooke's Law in assigned directions (in this case, in the medial/lateral directions, as well as in the anterior/posterior directions) between the nodes at each end of the spring. Spring displacement is measured as the relative displacement between the two nodes of the spring, and the force in the enforced directions is proportional to the displacement.

2.3.1.5. Springs Anisotropy

The Springs Anisotropy model was identical to the Springs model, however, the meniscus was given anisotropic properties (Table 2.2), identical to those of the Tied Anisotropy model. A summary of model properties and parameters can be found in Tables 2.1-2.3.

Table 2.1 Meniscus models used in this study and the interaction of each with the tibial plateau cartilage from least complex (Merged) to most complex (Springs/Anisotropic).

Model	Meniscus Interaction	Used Prior
Merged	Meniscus merged with tibial cartilage to form one structure (Figure 5)	McErlain
Tied	Meniscus manually tied to tibial cartilage (Figure 6)	Pena
Tied/Anistropic	Meniscus tied and given anistropic properties (Figure 6)	Papaioannou
Springs	Meniscus constrained to tibial cartilage by springs (Figure 7)	McErlain, Pena
Springs/Anisotropic	Springs model but with meniscal anistropic properties (Figure 7)	Kiapour

Table 2.2 Meniscus material properties, as well as the spring stiffness used in the spring interaction models.

Model	Modulus (MPa)	Poisson's Ratio	Spring Constant (N/mm)	Reference
Merged	40	0.45	-	Donahue
Tied	40	0.45	-	Donahue
Tied/Anisotropic	E1,E3 = 20 and E2 = 120	v1,v3 = 0.3 and v2 = 0.45	-	Mootanah, Kiapour
Springs	40	0.45	20	Donahue
Springs/Anisotropic	E1,E3 = 20 and E2 = 120	v1,v3 = 0.3 and v2 = 0.45	20	Mootanah, Kiapour

Table 2.3 Summary of all the material properties used in each model.

Structure	Young's Modulus (MPa)	Poisson's Ratio	Reference
Bone	50 - 21000	0.3	Wirtz
Cartilage	25	0.45	Mootanah
Meniscus	See Table 2	See Table 2	-
Ligaments	345	0.45	Butler

For each model, the meniscal horns were tied to the tibia, and the PCL was tied to the femur. All other structures either had shared nodes from the mesh generation, or were unconstrained and were included in the ABAQUS general contact formulation.

The loading boundary condition for each model was a uniform surface pressure placed on the proximal femur, equivalent to a 3000 N force. The distal tibia was completely constrained (U1, U2, U3, UR1, UR2, UR3 = 0), and the femur was constrained to allow all three translations, but no rotations (UR1, UR2, UR3 = 0). Contact was modeled as frictionless and a "penalty" was enforced for overclosure. The penalty is a force acting against the penetrating surface and is governed by Hooke's Law. The stiffness is chosen automatically by the ABAQUS solver and is based on the underlying element stiffness (overclosure stiffness defaults to ten times larger than the stiffness in ABAQUS). Therefore, the force applied is equal to the stiffness generated multiplied by the penetration distance (averaged across the surface if multiple nodes have penetrated)

2.3.2. Convergence Study

We performed a convergence analysis to verify the numerical accuracy of the model (adequate mesh density). Jones et al. demonstrated in a finite element study of the spine that an appropriate convergence criteria is a <5% difference in PDE solution from one mesh density to the next [10]. In our study, our convergence percentages are based on the difference from the highest resolution, as we assume this value to be the most accurate. In most knee models, bone element size is held constant, and the soft tissues are made finer and finer until convergence has been demonstrated for stress in soft tissues of interest. However, bone stresses, more specifically those in our region of interest, are a desired output variable. Therefore, the bone mesh in the region of interest was refined along with the cartilage and menisci meshes for this part of the study.

Beginning with an element edge length of 1.75 mm for the aforementioned structures, a mesh refinement of 0.25 mm edge length was made down to an edge length of 0.75 mm. The models were analyzed with the same boundary conditions as those done in the first study. Von Mises stresses (from each element), average maximum principal stresses, as well as the top 5% maximum principal stresses were obtained and compared for each model and for each mesh refinement. The solution from a single model, Springs Anisotropy, with quadratic elements (C3D10) was also analysed to investigate error associated with strain locking in linear tetrahedral elements.

2.3.3. Meniscal Attachment Complexity Comparisons

Using the converged states for each output variable, Von Mises stresses and maximum principal bone stresses for the femoral region of interest were obtained from each model. These stresses were compared between the levels of meniscal attachment complexity. Also tracked was the wall clock time taken for each analysis.

2.3.4. Material Property Sensitivity Analysis

We also investigated the effects of changing the material properties (bone, femoral cartilage, or meniscus) on the output stress in the bone (MFC) region of interest and the stress in the medial femoral cartilage. Using the Springs Anisotropy model described above, the bone material properties was significantly simplified by using only two material properties (trabecular E = 400 MPa, cortical E = 20,000 MPa) [9] (Figure 2.8) and then made more complex with 50 material properties. The cartilage was also changed to encompass a broader range of possible values (changed from 25 MPa to 7 MPa) [21], and the meniscus was changed from anisotropic to a softer, isotropic property (see Table 2.2, Springs vs. Springs Anisotropy). The same

load/displacement boundary conditions as previously described were implemented with these models, but only Von Mises stresses were evaluated as the output variable. This part of the study illustrated the importance of understanding the relationship between input variables and output variables. More specifically, the goal was to illustrate the importance of material properties, depending on the desired output.

Figure 2.8 Slice of the segmented femur (Simpleware) used to create the simplified bone properties. Trabecular bone is shown in blue and cortical bone is shown in light yellow.

2.4. Results

2.4.1. Convergence Study

For the average max principal stress data, convergence was achieved at 1.25 mm edge length resolution (Table 2.4). For the top 5% max principal stress data, convergence was achieved at 1 mm edge length resolution (Table 2.5). Lastly, convergence was achieved at 1.5 mm edge length resolution for Von Mises stress data (Table 2.6).

Table 2.4 Convergence analysis results for average maximum principal stress values taken from the femoral bone region of interest. Except for a slight discrepancy in the Springs model, for average stresses, convergence was achieved at an edge length of 1.25 mm.

	Average Tension					Average Compression				
Model / Edge Length (mm)	**1.75**	**1.5**	**1.25**	**1**	**0.75**	**1.75**	**1.5**	**1.25**	**1**	**0.75**
Merged	35%	7%	4%	1%	-	30%	0%	1%	1%	-
Tied	7%	6%	3%	2%	-	1%	1%	0%	0%	-
Tied Anisotropy	7%	6%	4%	2%	-	0%	1%	0%	1%	-
Springs	2%	2%	6%	3%	-	1%	1%	1%	2%	-
Springs Anisotropy	5%	4%	5%	2%	-	3%	0%	1%	0%	-

Table 2.5 Convergence analysis results for the top 5% maximum principal stress values taken from the femoral bone region of interest. Except for a discrepancy in the Springs model, convergence was achieved at an edge length of 1.00 mm.

	Top 5% Tension					Top 5% Compression				
Model / Edge Length (mm)	**1.75**	**1.5**	**1.25**	**1**	**0.75**	**1.75**	**1.5**	**1.25**	**1**	**0.75**
Merged	51%	7%	9%	2%	-	24%	3%	4%	2%	-
Tied	15%	6%	7%	4%	-	5%	2%	4%	2%	-
Tied Anisotropy	13%	6%	7%	4%	-	7%	3%	4%	3%	-
Springs	9%	3%	7%	3%	-	5%	3%	8%	6%	-
Springs Anisotropy	11%	5%	8%	2%	-	6%	4%	6%	3%	-

Table 2.6 Convergence analysis for average Von Mises stresses taken from the femoral bone region of interest. Convergence was achieved at 1.5 mm average edge length.

	Average Von Mises				
Model / Edge Length (mm)	**1.75**	**1.5**	**1.25**	**1**	**0.75**
Merged	31%	0%	0%	1%	-
Tied	0%	1%	0%	0%	-
Tied Anisotropy	0%	0%	1%	1%	-
Springs	1%	4%	2%	4%	-
Springs Anisotropy	2%	1%	1%	0%	-

In addition, use of quadratic elements with the Springs Anisotropy model resulted in only a 1% change in all output parameters, while wall clock time increased nearly tenfold.

2.4.2. Complexity of Meniscal Attachment

Average of the maximum (tensile) principal stress data taken from the femoral region of interest shows that the addition of springs made the only significant difference in output stresses (Table 2.7). Tensile stress values increased by ~20%, though compressive stresses remained about the same (~2% change), with Tied Anisotropy showing an 8% error (Table 2.7). The top 5% of maximum (tensile) principal stress data from the femoral region of interest again showed that the addition of springs created changes in the tensile stress values, and these values were increased by ~25% (Table 2.7). However, when looking at the Von Mises stress data, with the exception of the Tied Anisotropy model, we observe a less than 5% difference in average stress between all models, most notably nearly identical average stresses between the most basic (Merged) and the most complex (Springs Anisotropy) (Table 2.7). The wall clock time for the Merged model was substantially lower than the other models (~30%), while there was no notable difference between wallclock times for the other models.

Table 2.7 Stress data (MPa) from the femoral bone region of interest using the 1.00 mm edge length resolution (converged for all outputs).

	Avg. Tension	Avg. Compression	Top 5% Tension	Top 5% Compression	Avg. Von Mises
Merged	0.2238	1.7564	0.5726	3.4099	1.7243
Tied	0.2315	1.7658	0.5892	3.6205	1.761
Tied Anisotropy	0.2185	1.5911	0.6017	3.0538	1.5725
Springs	0.3148	1.6931	0.8417	3.3441	1.7917
Springs Anisotropy	0.2816	1.7329	0.7745	3.2309	1.7283

2.4.3. Material Properties Sensitivity Analysis

When bone stresses are the desired output variable, specifically Von Mises for this study, changing the bone properties from a complex, mapped spectrum to simple two-level properties of trabecular and cortical bone has a substantial impact on the results (67%). However, increasing the number of levels bone properties resulted in an insignificant change (~1%) (Table 2.8). Changing the meniscus or cartilage properties results in a <5% change in bone stresses (Table 2.8). However, when stresses in the femoral cartilage are the desired output variable, the change in cartilage properties from 25 MPa to 7 MPa resulted in an 11% change in average stress. Changing the meniscus properties from stiff, anisotropic to soft, isotropic properties and changing the bone properties to the two-level definition resulted in a <5% change in cartilage stress (Table 2.8).

Table 2.8 Results from the material properties sensitivity analysis. The structure column indicates the structure undergoing a change from the Springs Anisotropy model. The Change column describes the specific change being made. The percentages shown are the differences in Von Mises (VM) stress that resulted from material property change, when compared with the Springs Anisotropy model.

Structure	Change	Bone VM	Femoral Cartilage VM
Meniscus	E = 40 MPa	4%	1%
Bone	2 levels of bone properties	67%	3%
Bone	50 levels of bone properties	1%	2%
Cartilage	E = 7 MPa	1%	11%

2.5. Discussion

With computational power continually increasing, the use of computation in biological phenomena continues to increase, and the complexity and size of models is also increasing. With higher complexity comes better model fidelity, but also an increased probability for errors, typically arising from the solver taking shortcuts to handle the added complexity (i.e, approximating a nonsymmetric Jacobian matrix with a symmetric matrix). The computational investigator has the duty to perform necessary verification and validation studies to ensure that the results are accurate and meaningful.

This study examined several aspects of complexity for a model of the equine stifle joint, and established preferred levels of mesh refinement, meniscal restraint, and material property complexity. We have shown that for medial femoral condyle bone stresses, the most complex meniscal attachment is important (as other methods underestimate), accurate bone material

properties are crucial, and soft tissue properties have only a small effect on the results of the model.

We have clearly illustrated that the output variables should dictate the accuracy and complexity of input variables/parameters. Sensitivity to these inputs should be verified and the model validated for each study. For example, our data shows that our hierarchy of model complexity for meniscal attachment presents additional tensile max principal stresses in the femur with the introduction of springs connecting the meniscus to the tibial cartilage (Table 2.7), yet compressive stresses remain relatively unchanged. Because our objective is to investigate bone damage, the tensile stresses are thus incredibly important. Therefore, future work on our equine stifle model will include a spring interaction between the meniscus and tibial cartilage. However, one could easily use a much simpler model, such as the Merged model, if compressive stresses or Von Mises stresses were the primary concern, and both model preparation time and computational time would be drastically reduced. The Merged model eliminates the need for proper delineation of tibial cartilage and meniscus, thus the segmentation process becomes less tedious and indirectly less prone to geometric error since the geometry of the combined part is simplified. However, combining parts can create severe curvature, resulting in error. The transition between the meniscus and the tibial cartilage along the periphery creates this severe curvature. This error, prominently seen in the 1.75 mm edge length model, can be attenuated by finding an appropriate element size that smooths the geometry of the part.

We also observed that mesh convergence depends on the output variable used. This finding is consistent with Tseng's recent findings in their convergence research of a skull model [22]. It may seem plausible that if convergence is achieved at a certain mesh density when looking at Von Mises stresses, the same mesh density would then work for other output

parameters such as max principal stresses. As shown in Tables 2.4-2.6, this is not a safe assumption to make. The implication then is that convergence must be shown for each desired output variable, and a mesh density should then be selected to obtain accuracy in all output variables. Based on this study, we will use an edge length of 1.00 mm for future studies as this edge length is converged for all parameters.

This emphasis on output parameter is also important. With our focus on bone stresses, we see that meniscal and cartilage changes have little effect on the measured bone stress (Table 2.8). If we were to look at femoral cartilage stress, or contact pressure, the accuracy of cartilage properties would greatly affect the results (Table 2.8). We also showed that increasing the number of bone properties from 20 to 50 (evenly distributed between 50 MPa-21,000 MPa) resulted in an insignificant change, thus the use of 20 properties is sufficient. This finding is interesting in light of other studies that put great emphasis on the number of bone properties. McErlain et al. used theoretical approaches in selecting the number of bone properties used, resulting in more than 600 levels of properties [23].

For analysing bone stresses, errors in the bone properties will greatly influence our results (Table 2.8). It's important to note that the bone property mapping is subject to error from the CT data itself. Ideally, a phantom would be present in the scan as a means of scaling the Hounsfield units [24]. Unfortunately, our working data set (as with many clinical images) does not contain such a phantom.

In our meniscal attachment study, we demonstrated that computational time is only reduced by using linear elements, and by using the Merged model (though it should be noted that we did not investigate the effects of reducing the number of quadratic elements used). This may be partially explained by ABAQUS not having to track any user-defined constraint. In both the

Tied and Springs models, manual constraints were made in ABAQUS CAE, whereas the Merged model simply had shared nodes between the meniscus and tibial cartilage (and it is modeled as one structure). Because the nodes were shared, no constraint had to be created. Computational time is impacted the same way whether a tie constraint is being tracked, or a spring interaction, indicating that there is no computational time advantage in using a tied constraint over a spring constraint.

We acknowledge that this study has limited scope and several limitations. All models were based on one CT scan of one stifle joint. Thus, there is some possibility that certain results may not be generalizable. In addition, the study of material property sensitivity was limited to a few levels of material properties, and a more complete analysis may yield further insight.

2.6. Conclusion

This paper was intended for the primary goal of establishing and verifying the proper mesh refinement and complexity of the stifle joint. The results indicate the importance of a thorough mesh convergence study, selecting appropriate meniscal attachment in a knee model, and the importance of material properties for obtaining accurate data from a model.

2.7. References

[1] Henninger, H. B., Reese, S. P., Anderson, A. E., and Weiss, J. A., 2010, "Validation of Computational Models in Biomechanics," Proc Inst Mech Eng H, 224(7), pp. 801-12.

[2] Courant, R., 1943, "Variational Method for the Solution of Problems of Equilibrium and Vibrations," Am. Math Soc, 49), pp. 1-43.

[3] Martin, H., 1966, "Introduction to Matrix Methods of Structural Analysis," McGraw-Hill, pp.

[4] Davids, N., and Mani, M. K., 1972, "Effects of Turbulence on Blood Flow Explored by Finite Element Analysis," Computers in Biology and Medicine, 2(4), pp. 311-319.

[5] Belytschko, T., Kulak, R. F., Schultz, A. B., and Galante, J. O., 1974, "Finite Element Stress Analysis of an Intervertebral Disc," Journal of Biomechanics, 7(3), pp. 277-285.

[6] Rybicki, E. F., and Simonen, F. A., 1977, "Mechanics of Oblique Fracture Fixation Using a Finite-Element Model," Journal of Biomechanics, 10(2), pp. 141-148.

[7] Hull, M. L., 2002, "A Finite Element Model of the Human Knee Joint for the Study of Tibio-Femoral Contact," Journal of Biomechanical Engineering, 124(3), pp. 273.

[8] Mootanah, R., Imhauser, C. W., Reisse, F., Carpanen, D., Walker, R. W., Koff, M. F., Lenhoff, M. W., Rozbruch, S. R., Fragomen, A. T., Dewan, Z., Kirane, Y. M., Cheah, K., Dowell, J. K., and Hillstrom, H. J., 2014, "Development and Validation of a Computational Model of the Knee Joint for the Evaluation of Surgical Treatments for Osteoarthritis," Comput Methods Biomech Biomed Engin, 17(13), pp. 1502-17.

[9] Kiapour, A., Kiapour, A. M., Kaul, V., Quatman, C. E., Wordeman, S. C., Hewett, T. E., Demetropoulos, C. K., and Goel, V. K., 2014, "Finite Element Model of the Knee for Investigation of Injury Mechanisms: Development and Validation," J Biomech Eng, 136(1), pp. 011002.

[10] Kazemi, M., Dabiri, Y., and Li, L. P., 2013, "Recent Advances in Computational Mechanics of the Human Knee Joint," Comput Math Methods Med, 2013(pp. 718423.

[11] Joshi, M. D., Suh, J. K., Marui, T., and Woo, S. L., 1995, "Interspecies Variation of Compressive Biomechanical Properties of the Meniscus," J Biomed Mater Res, 29(7), pp. 823-8.

[12] Weiss, J. A., Gardiner, J. C., Ellis, B. J., Lujan, T. J., and Phatak, N. S., 2005, "Three-Dimensional Finite Element Modeling of Ligaments: Technical Aspects," Medical Engineering & Physics, 27(10), pp. 845-861.

[13] Jeffcott, L. B., Kold, S. E., and Melsen, F., 1983, "Aspects of the Pathology of Stifle Bone Cysts in the Horse," Equine Vet J, 15(4), pp. 304-11.

[14] Santschi, E. M., Williams, J. M., Morgan, J. W., Johnson, C. R., Bertone, A. L., and Juzwiak, J. S., 2015, "Preliminary Investigation of the Treatment of Equine Medial Femoral Condylar Subchondral Cystic Lesions with a Transcondylar Screw," Vet Surg, 44(3), pp. 281-8.

[15] Pena, E., Calvo, B., Martinez, M. A., and Doblare, M., 2006, "A Three-Dimensional Finite Element Analysis of the Combined Behavior of Ligaments and Menisci in the Healthy Human Knee Joint," J Biomech, 39(9), pp. 1686-701.

[16] Papaioannou, G., Demetropoulos, C. K., and King, Y. H., 2010, "Predicting the Effects of Knee Focal Articular Surface Injury with a Patient-Specific Finite Element Model," The Knee, 17(1), pp. 61-68.

[17] Donahue, T. L. H., Hull, M. L., Rashid, M. M., and Jacobs, C. R., 2003, "How the Stiffness of Meniscal Attachments and Meniscal Material Properties Affect Tibio-Femoral Contact Pressure Computed Using a Validated Finite Element Model of the Human Knee Joint," J Biomech, 36(1), pp. 19-34.

[18] Wirtz, D. C., Schiffers, N., Pandorf, T., Radermacher, K., Weichert, D., and Forst, R., 2000, "Critical Evaluation of Known Bone Material Properties to Realize Anisotropic Fe-Simulation of the Proximal Femur," J Biomech, 33(10), pp. 1325-30.

[19] Butler, D. L., Kay, M. D., and Stouffer, D. C., 1986, "Comparison of Material Properties in Fascicle-Bone Units from Human Patellar Tendon and Knee Ligaments," Journal of Biomechanics, 19(6), pp. 425-432.

[20] Jones, A. C., and Wilcox, R. K., 2008, "Finite Element Analysis of the Spine: Towards a Framework of Verification, Validation and Sensitivity Analysis," Med Eng Phys, 30(10), pp. 1287-304.

[21] Laasanen, M. S., Toyras, J., Korhonen, R. K., Rieppo, J., Saarakkala, S., Nieminen, M. T., Hirvonen, J., and Jurvelin, J. S., 2003, "Biomechanical Properties of Knee Articular Cartilage," Biorheology, 40(1-3), pp. 133-40.

[22] Tseng, Z. J., and Flynn, J. J., 2015, "Convergence Analysis of a Finite Element Skull Model of Herpestes Javanicus (Carnivora, Mammalia): Implications for Robust Comparative Inferences of Biomechanical Function," J Theor Biol, 365(pp. 112-48.

[23] Mcerlain, D. D., Milner, J. S., Ivanov, T. G., Jencikova-Celerin, L., Pollmann, S. I., and Holdsworth, D. W., 2011, "Subchondral Cysts Create Increased Intra-Osseous Stress in Early Knee Oa: A Finite Element Analysis Using Simulated Lesions," Bone, 48(3), pp. 639-46.

[24] Mah, P., Reeves, T. E., and Mcdavid, W. D., 2010, "Deriving Hounsfield Units Using Grey Levels in Cone Beam Computed Tomography," Dentomaxillofac Radiol, 39(6), pp. 323-35.

3. Stresses Associated with Subchondral Bone Cysts in an Extended Equine Stifle

3.1. Introduction

Subchondral lucencies (SCL) occur in the medial femoral condyle (MFC) of horses and can cause lameness [1-4] (Figure 3.1). They are more common in horses ≤ 2 years of age, but can occur in older horses. The causes of SCL are not well understood, however, trauma and osteochondrosis are most commonly implicated [3, 4]. Serial radiographs of young horses that develop SCLs indicate initial trabecular bone sclerosis at the central area of femoro-tibial contact in extension followed quickly by MFC flattening, and then progressive loss of subchondral trabecular bone resulting in a SCL. Histologic examination of SCL contents reveals fibroplasia and capillary proliferation as well as fibrous tissue, degenerated bone and cartilage and disorganized areas of granulation tissue and woven bone [5, 6]. Biochemical analysis of the tissue lining the SCL removed arthroscopically reveals that inflammatory cytokines associated with bone resorption are present, and likely play a role in SCL formation and lameness [7, 8].

Figure 3.1 Radiograph of a grade 3 MFC SCL from a young Thoroughbred [9].

Treatments of SCL are directed at reducing local inflammation and promoting bone and cartilage healing. Injection of the SCL lining with corticosteroids can be used to reduce

inflammation [10], however arthroscopic SCL debridement of articular cartilage, disorganized SCL tissue including the lining is considered the treatment of choice [11-13]. After debridement, SCL voids can be left open, or filled with cancellous bone, osteochondral grafts [14], or a combination of bone substitutes, growth factors, chondrocyte grafts and mesenchymal stem cells in fibrin glue [15]. Treatment success rates range between slightly >50% to slightly <75%, with a tendency for surgical procedures to provide a somewhat better result than conservative treatment [1, 2, 6, 9-16]. However, there is little data about bone healing after debridement, and what is available suggests it occurs in < 20% of patients [15]. Given this poor rate of radiographic healing, the lack of data on the long-term resolution of lameness leaves doubt about the efficacy of this treatment approach.

Recently, treatment of MFC SCL using a lag screw has been reported that improves the rate of lameness resolution, and is the first treatment to report significant and consistent bone healing [9]. This suggests that a biomechanical approach can improve the treatment of equine SCL, but very little is known about the stresses within the medial femoral condyle, and how the procedure may be optimized. The equine stifle is a complex biological system and direct collection of biomechanical data would be difficult, if not impossible. Computational biomechanics provides a unique and powerful approach in overcoming this hurdle. The objective of the present study is to investigate the stresses in the medial femoral condyle at three different grades of SCL progression using finite element analysis. This information can help us better understand the mechanics associated with SCL that will allow clinicians to develop and implement rational treatment strategies. For this study, the grading scale of SCL defect presented in the introduction has been slightly modified to clearly distinguish cystic models from pre-cystic models, as well as generalizing the cystic development process into three stages. G1 in this study

correlates to a Grade 1-Grade 2 defect, G2 correlates to a Grade 3 defect, and G3 correlates to a Grade 5 defect.

3.2. Methods

There is no available cross-sectional imaging data (CT and/or MRI) of MFC SCL progression from the intact condition to development of a large defect, and this presents a challenge for the creation of a MFC SCL model. Fortunately, descriptive literature (including radiographs) is available detailing SCL progression, which has resulted in a grading scale of SCL progression. Therefore, this study is able to take advantage of universally recognized clinical aspects of subchondral bone lesions. By creating an anatomically accurate model of a healthy stifle joint, manipulations can be made that mimic the stages of SCL progression, and the biomechanics associated with stifle injury (SBCs in this study) can be modeled and analyzed. This study incorporates a total of 11 models, separated into two model trees (one with a flattened femur, and one without) that represent clinically apparent aspects of SCL development. The lack of literature addressing flattened femurs make it an interesting aspect of MFC injury to isolate.

3.2.1. Segmentation and Meshing

Computerized tomography (CT) images (247x247x130 voxels, 0.5, 0.5, 0.5 mm spacing) of an extended equine stifle joint were used as the canvas to segment both bony and soft tissue structures using ScanIP v7.0 (Simpleware, United Kingdom). The CT scan used in this study was resampled to a finer resolution than was used in Chapter 2 in order to have finer control over model manipulations (making the femur flat, for example).

To correctly segment soft tissues without MRI data, reasonable assumptions were made for soft tissue boundaries. For example, it is known that the articular cartilage in the stifle joint

has a thickness of about two mm [17]. Therefore, the segmented bone can be dilated by two millimeters, and the original bone can be subtracted from the dilated structure, creating an even articular cartilage surface around each bone. An example of the segmentation process can be seen in Figure 3.2.

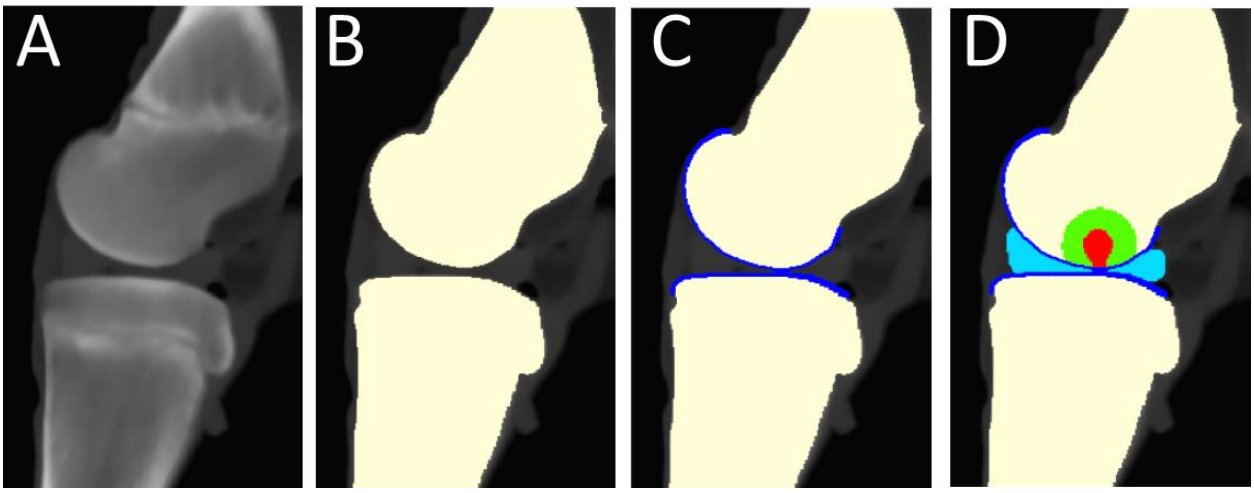

Figure 3.2 Segmentation pictures from the MFC sagittal plane. A) Unsegmented image revealing original CT data. B) Femur and tibia (tan) segmented using an automatic grayscale threshold tool. C) Cartilage (dark blue) added to the periphery of the bone using a dilation technique. D) Fully segmented slice with the region of interest (green), SCL (red), and the medial meniscus (light blue) added.

Furthermore, segmentation was performed under the supervision of a professor of veterinary surgery with detailed emphasis on clinical observations of stifle anatomy and pathology. Figure 3.3a is a frontal section of the cranial MFC that reveals that the axial MFC cartilage (articulates with the medial tibial eminence) is thicker than the abaxial cartilage (contacts the meniscus). This anatomy was reflected in the model (Figure 3.3b).

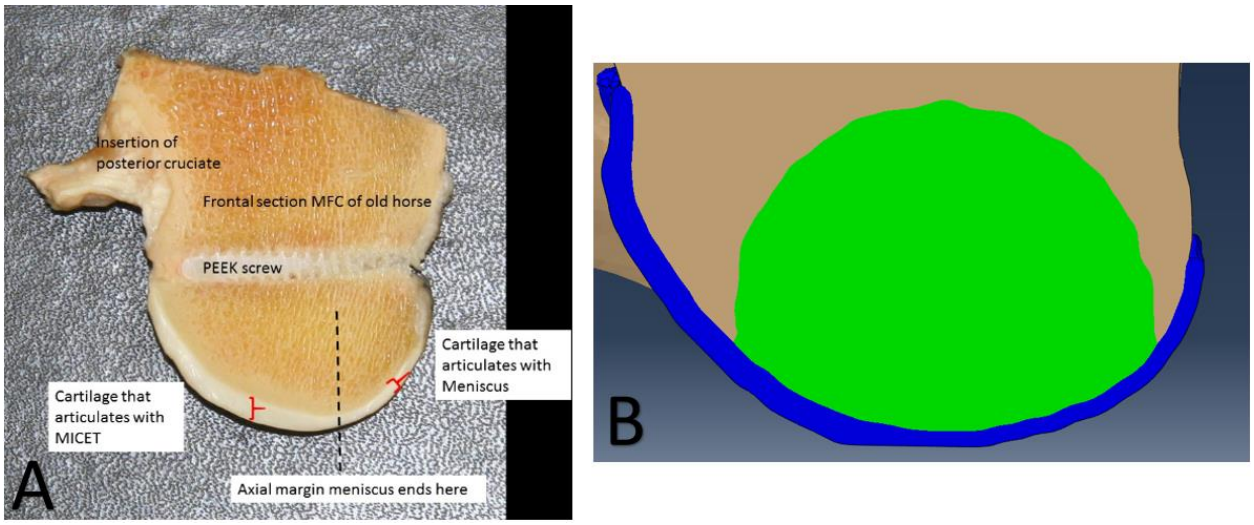

Figure 3.3 A) Frontal section of the medial condyle illustrating the thickened cartilage that articulates with the tibial eminence and B) the same frontal section of our finite element model with cartilage shown in blue.

Included structures in the finalized 3D geometry were the femur, tibia, articular cartilage, menisci, patella, distal patellar ligaments, and the posterior cruciate ligament (PCL). This geometry was then divided into piecewise linear tetrahedral elements using the FE Free meshing algorithm in ScanIP and subsequently exported into ABAQUS v6.14 (SIMULIA, Providence, RI) to fully develop a finite element model (Figure 3.4).

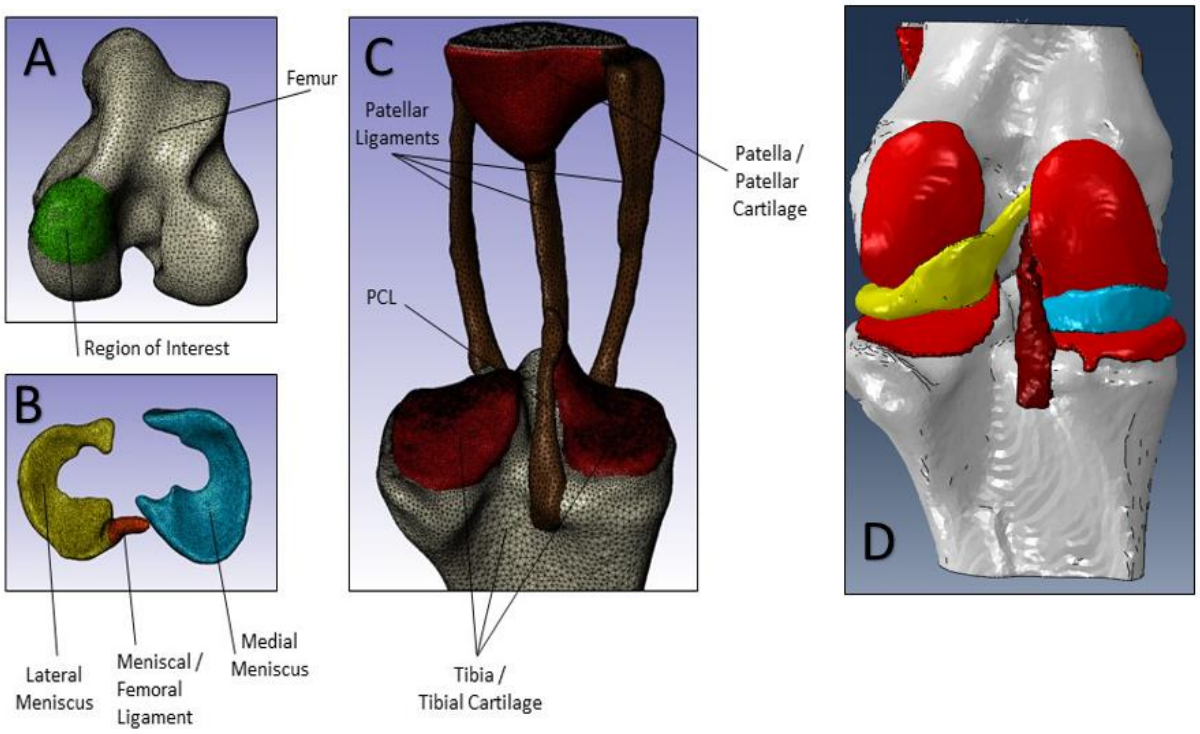

Figure 3.4 Finite element meshes generated from ScanIP and full assembly in ABAQUS. A) Distal femur (not shown is the femoral cartilage to reveal green region of interest in the MFC). B) Menisci and meniscal ligament attachment. C) Tibia, patella, patellar ligaments, and the PCL. D) Full model assembly.

3.2.2. Material Properties

For the present study, instantaneous stress responses were of primary concern, which allows for simplified material property formulations. With soft tissues such as cartilage having a viscoelastic time constant of 1500 seconds, the elastic solution does not differ from the biphasic solution in short loading times. Thus, linear elastic formulations that neglect viscoelasticity are appropriate for both accuracy and computational efficiency.

It has been shown that bone's moduli is dependent on its mass density [18-21]. Bone is a heterogenous structure and was therefore modeled with 20 levels of material properties. 20 levels were selected as a result of an investigational study our lab did to determine the amount at which output stresses became stable. Bone moduli were correlated with Hounsfield units from the CT scan using the following equations:

$$Mass\ Density = (1.067 * 10^{-3}) * GrayScale \quad (1)$$

$$Young's\ Modulus = (6.0 * 10^{3}) * MassDensity^{2.5} \quad (2)$$

The power of 2.5 for the modulus equation accounts for the wide range of bone densities, where $E \alpha \rho^3$ for high density bone and $E \alpha \rho^2$ for low density bone [19]. This resulted in Young's Modulus ranging from 50 MPa to 21,000 MPa. The cartilage was modeled as linear and isotropic with near incompressible behavior (Table 3.1). The meniscus was modeled as linear, anisotropic with different properties assigned to the circumferential, radial, and axial directions to account for its aligned collagen structure. Each meniscus was tied to their anatomical insertion points (meniscotibial ligaments), and the peripheral rim was attached to the tibial plateau using springs (k = 10 N/mm), which partially constrains meniscal motion similar to the joint capsule but allows for appropriate meniscal translation on the tibial plateau. The ligaments were modeled as linear and isotropic. Under our loading scheme, the collateral ligaments would not take on any compression, and the compressive resistance in the model would be inappropriate. The SCL was modeled as linear, isotropic and assigned a low Young's Modulus relative to the surrounding tissue, as well as a high Poisson's ratio to account for the incompressibility of the cystic contents. All material properties have been utilized in previous studies and are consistent with values

determined experimentally [22-28]. A summary of the material properties used can be found in Table 3.1.

3.2.3. Verification

By using commercially available finite element code (ABAQUS), verification of the code was unnecessary, as the developers have already done this. However, appropriate verification was performed to demonstrate appropriate mesh convergence. Demonstrating mesh convergence is a critical component to verifying the mathematical accuracy of a finite element model and shows that the model is not prone to errors from the mesh itself [29-32]. We used the benchmark of a <5% change in solution resolution between two successive meshes as an appropriate standard for convergence as described in a spine finite element model [33]. All structures were modeled initially with having an average element edge length of 2.00 mm. Soft tissues and the MFC ROI were refined by 0.25 mm increments until a <3% change was observed for all relevant output variables at an edge length of 1.00 mm. Use of quadratic elements in the model produced only a 1% deviation from linear elements.

3.2.4. Validation

Finite element models can be difficult to validate, especially when investigating phenomena that cannot be tested experimentally. While the bone stresses in the MFC cannot be validated with absolute certainty, a meaningful result can still be obtained through forms of indirect validation. We compared tibial contact pressure in the model with experimental data from a cadaveric stifle joint loaded in simple compression (Figure 3.5). Using the same boundary conditions, our model exhibited the same magnitude and distribution of stresses across the

medial plateau as the *ex vivo* results [34]. The femoral ROI for which we wish to generate bone stresses is immediately proximal to the medial tibial plateau. Therefore, it is reasonable to assume the load exerted on this region is accurate, and with the right material formulation, the bone stresses obtained should be valid.

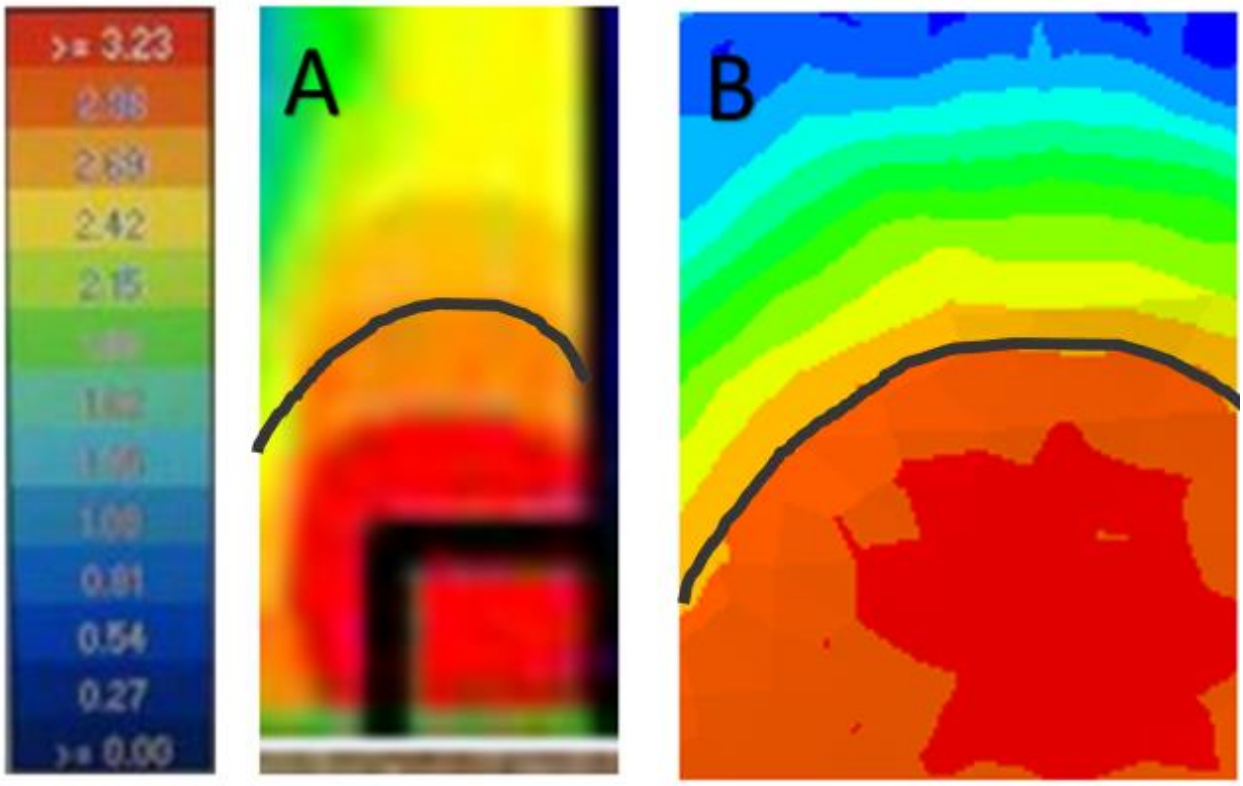

Figure 3.5 A) Ex vivo pressure distribution on the tibial plateau with cranial on the left of the image and caudal to the right [34]. B) Finite element model pressure distribution using the same boundary conditions as those used in A, as well as the same contact pressure scale on the left. The area immediately below the region of interest has been outlined in black in both images. Adapted from Veterinary Surgery, 2014;44:289-296 with permission.

Table 3.1 Summary of the material properties used in the current model.

Structure	Type	Young's Modulus (MPa)	Poisson's Ratio
Bone	Isotropic	50-21,000	0.3
Menisci	Anisotropic	Radial and Axial = 20 Circumferential = 120	Radial and Axial = 0.3 Circumferential = 0.45
Cartilage	Isotropic	25	0.45
Ligaments	Isotropic	300	0.3
SCL	Isotropic	1	0.49

3.2.5. Boundary Conditions

In order to accurately represent the contact mechanics of the stifle joint during loading, frictionless, nonlinear (surface-to-surface) contact formulations were defined between all articulating surfaces using the general contact formulation in ABAQUS. The femur was able to translate in all three anatomical planes but was constrained in flexion/extension as well as internal and external rotation (UR2, UR3 = 0). The distal tibia was fully constrained (encastre). A surface pressure was applied to the proximal femur, resulting in a total 3000 N force in the distal direction. This load approximates the load on a stifle joint during a walking task [35]. A 175 N tensile force was applied to the proximal patella to simulate the action of the quadriceps apparatus.

3.2.6. Analysis

All quantitative analysis of stress data from FEA was performed using customized scripts in Matlab R2014b (MathWorks) (Appendix). Stress data was extracted from the region of interest and exported to an excel spreadsheet, which was then read into Matlab. This data

included the maximum principal stresses, minimum principal stresses, Von Mises stresses, and maximum Tresca stresses (shear). All values reported are an average of the top 5% for each output, as the bone is most likely to fail in areas of significantly higher stresses. Included parenthetically in the results tables are the percent differences when compared with the Normal model.

During SCL development, a lucency occurs centrally at the joint surface in the sclerotic trabecular bone and the articular cartilage collapses [9]. Therefore, modeling the initial defect as a void with low modulus elements may be an inaccurate representation of the defect. In light of this, we performed a preliminary investigation of the effects of changing the grade 1 SCL into an area of collapsed bone and cartilage. Table 2 shows the changes in stress between the two methods of modeling the defect.

Table 3.2 Comparative stresses (MPa) between the collapsed bone model and the G1 model. Both have the same area of defect, but the G1 model retains the same model geometry with elements in the defect having low properties, whereas in the collapsed bone model, cartilage has been collapsed into the defect to retain its integration with the bone. Though a 5% change in stress was found in compression between the two models, this is an acceptable difference and both models compared to the Normal model had a lower difference (<3%).

	Tension (MPa)	**Shear (MPa)**	**Von Mises (MPa)**	**Compression(MPa)**
G1	0.8396	4.3042	3.7862	4.491
Collapsed	0.8434	4.4793	3.9453	4.729
% Change	0%	4%	4%	5%

Because the G1 model had a negligible effect on stresses compared to the collapsed bone model, it was used in further analyses, as it is much easier to implement. The small increases in stress in the collapsed model expected because the SCL of the G1 model was assigned a modulus of 1 MPa. Very little load is conveyed through the SCL, but enough is transferred to slightly lower the stresses in the ROI. However, creating models with idealized SCL structures was much less time-intensive than collapsing the bone and re-segmenting the cartilage. Also, the element quality around sharp bends may have lower quality, and the geometry of collapsed cartilage in Grade 2 or 3 cysts is less clear and may vary substantially.

MFC finite element models were tested on two geometries, normal and flattened. Both normal and flattened geometries were tested because many MFC with radiographic abnormalities have flattening at the area of MFC and tibial contact in extension. In the flattened model, the MFC was flattened ~1 mm (depth) and 10mm (width) to mimic observed radiographic and post-mortem flattening (Figures 3.6-3.7). The first trials were of normal MFC geometry. Sclerosis is the first radiographic abnormality detected in young horses and was added to normal geometry by increasing the bone modulus 12.8% [36]. Sclerosis was retained in further trials in normal geometry including G1, G2 and G3 defects. Defect size was chosen to depict conservative estimates of naturally occurring voids. In this study, grade 1 (G1) is a small central MFC depression (~0.03 cm^3) in subchondral bone, grade 2 (G2) is a larger domed (~0.5 cm^3) defect with a large articular opening, and grade 3 (G3) is a larger bone defect (~1.00 cm^3) with a smaller articular footprint. Radiographic images for each defect can be seen in Figure 3.8. Defect size and location, and the region of interest (ROI) is schematically represented in Figure 3.9. The second set of trials was performed with sclerosis and flattened MFC geometry and with G1-3 defects.

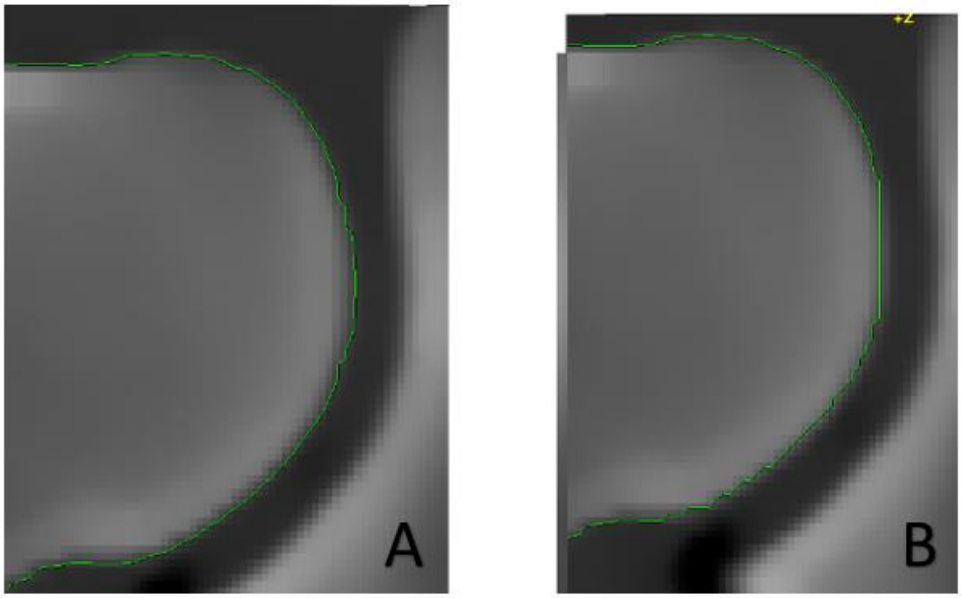

Figure 3.6 A) Normal contour generated by ScanIP showing the surface used by the meshing algorithm. B) Flattened contour to the right (distal). Note the flattening at the articulation site as well as the articulation site with the medial tibial eminence (lower right).

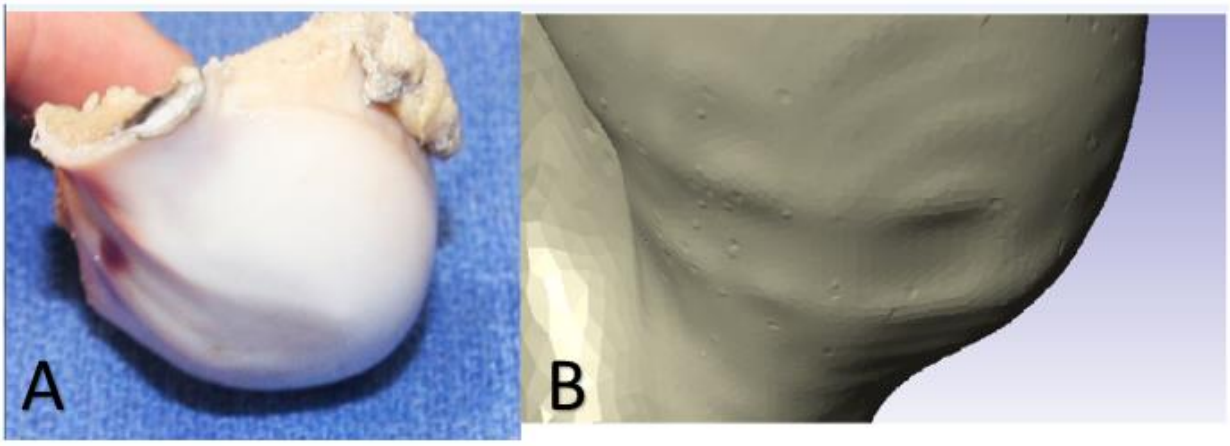

Figure 3.7 A) Flattened MFC. B) Model preview after implementing the flattening in ScanIP. Note the "rim" around the flattening in the actual femur and the model preview. Though the rim is exaggerated in the preview tool, it is appropriately smoothed in the actual mesh.

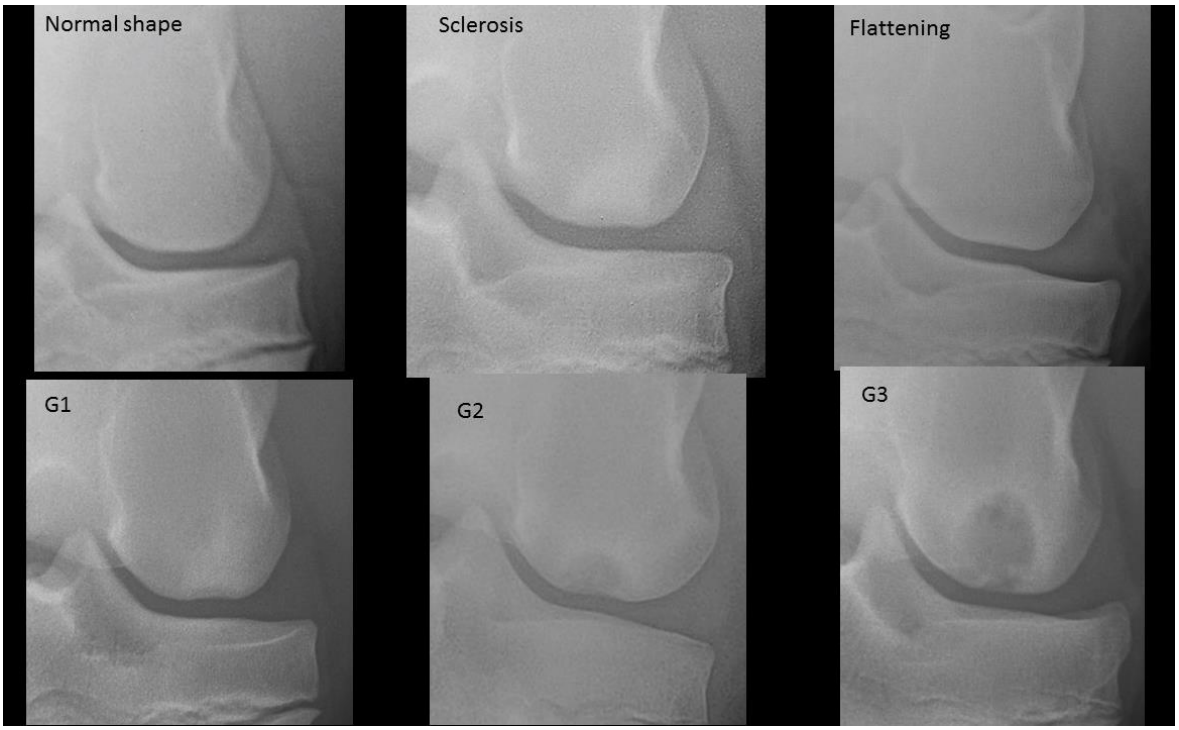

Figure 3.8 Caudo-cranial radiographic images of six conditions tested in the finite element model.

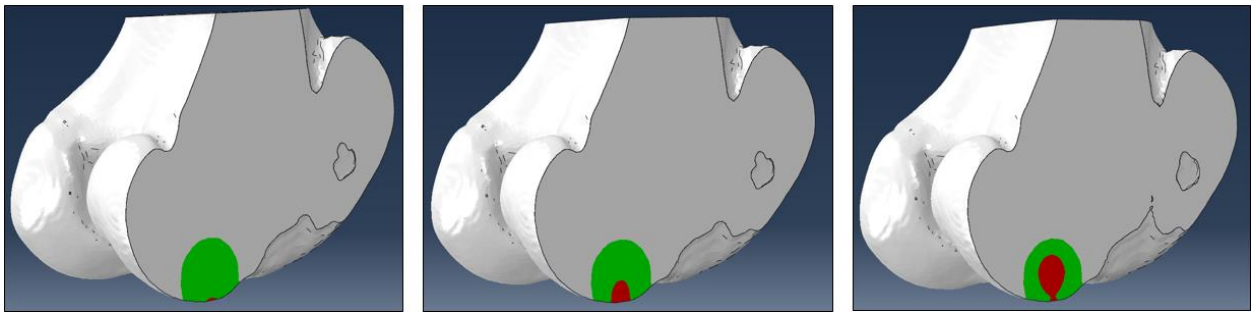

Figure 3.9 Isometric projections of three SCL models with the femoral region of interest shown in green and the SCL in red. For the purpose of this study, a grading scheme of 1-3 was utilized to simulate SCLs representing a small shallow defect (G1), a mid-size defect (G2), and a larger (G3) SCL.

3.3. Results

Each finite element model required approximately three hours to converge on a solution using 8 cores of an i7-3960X CPU @ 3.30 GHz. Predicted stresses and the percentage change from the normal condition (healthy MFC) were calculated for a MFC with normal geometry (Table 3) and with central MFC flattening (Table 4).

3.3.1. Stress measurements

Compressive, tensile, shear, and von Mises stress in the top 5% of elements in each MFC model varied with MFC condition (Table 3.3). The addition of sclerosis to normal MFC geometry increased all predicted stresses approximately 14%. Compared to the normal model, flattening caused a decrease in predicted compressive, shear and von Mises stresses by 27%, and an increase of 9% in tensile forces. A G1 defect without a flattened condyle decreased predicted compressive, shear and von Mises stress in the normal MFC approximately 20% but did not affect tension any more than the sclerotic model. In the flattened MFC (Table 3.4), a G1 defect compared to the normal geometry decreased compressive, shear and von Mises stress approximately 15%, and tensile stress rose 29%. A G2 defect in the normal MFC still had a decrease in predicted stress for compression, shear and von Mises, yet tensile stress increased further to 37% above what is seen in a normal MFC. A G2 defect in the flattened MFC increased compressive, shear and von Mises stress approximately 3%, and tensile stress increased to 45% higher than normal. A G3 defect in the normal MFC increased compression, shear and von Mises stress approximately 5% above normal, and tension 74%. A G3 defect in the flattened MFC increased compressive, shear and von Mises stress approximately 25%, and tensile stress increased 102% compared to a normal geometry. Although all predicted stresses decreased in an

intact MFC when flattened, all stresses for all defects were increased in a flattened MFC as compared to a normal MFC.

Table 3.3 Compression, tension, shear and von Mises stresses in the top 5% of all elements by condition in a medial femoral condyle with normal geometry. G1-G3 are increasing sizes of defects. Parenthetically shown is the percentage change when compared with the normal MFC.

	Compression MPa (% change)	**Tension MPa (% change)**	**Shear MPa (% change)**	**von Mises MPa (% change)**
Normal	5.3187	0.6519	4.9669	4.529
Sclerotic	6.11 (15%)	0.76 (17%)	5.54 (11%)	5.08 (12%)
G1	4.23 (-21%)	0.76 (17%)	4.05 (-18%)	3.65 (-19%)
G2	4.55 (-15%)	0.89 (37%)	4.47 (-10%)	3.97 (-12%)
G3	5.56 (4%)	1.13 (74%)	5.30 (7%)	4.82 (6%)

Table 3.4 Comparison of compression, tension, shear and von Mises stresses in the top 5% of all elements by condition in a medial femoral condyle with normal and flattened femur geometry. G1-G3 are increasing sizes of defects.

	Compression (% change)	**Tension MPa (% change)**	**Shear MPa (% change)**	**von Mises MPa (% change)**
Normal	5.3187	0.6519	4.9669	4.529
Sclerotic	6.11 (15%)	0.76 (17%)	5.54 (11%)	5.08 (12%)
Flattened	3.91 (-27%)	0.71 (9%)	3.65 (-27%)	3.33 (-27%)
G1	4.49 (-16%)	0.84 (29%)	4.30 (-13%)	3.79 (-16%)
G2	5.37 (1%)	0.95 (45%)	5.28 (6%)	4.64 (2%)
G3	6.31 (19%)	1.32 (102%)	6.44 (30%)	5.85 (29%)

3.3.2. Stress mapping

Stress mapping was performed for flattened MFC geometry for compression, tension, and shear stresses in the frontal and sagittal planes. The frontal plane was located at the site of femoral-tibial contact and the sagittal plane was the center of the MFC. Tensile stress was low for the normal, sclerotic and flattened conditions in both the frontal and sagittal planes (Figure 3.10). However, focal areas of tensile stress were predicted for all three defects (primarily in the frontal plane), enlarged with defect size, and for the G3 defect, were largest at the proximal-medial and distal-lateral aspects (Figure 3.10). Shear stress was elevated in the normal and sclerotic conditions at the femoro-tibial contact zone and were highest in the sagittal plane. Shear stress decreased with flattening and the G1 defect, increased with G2 and G3 defects in both planes, and were largest distally and laterally (Figures 3.11-3.12). Compression demonstrated a similar pattern as shear, elevated at the contact zone in both the frontal and sagittal planes in normal and sclerotic models and decreasing with flattening and the G1 defect (Figures 3.13-3.14). High compressive stress was predicted with G2 and G3 defects distally at the contact zone in both planes. Both shear and compressive stress were very low at the proximal aspect of the G3 defect.

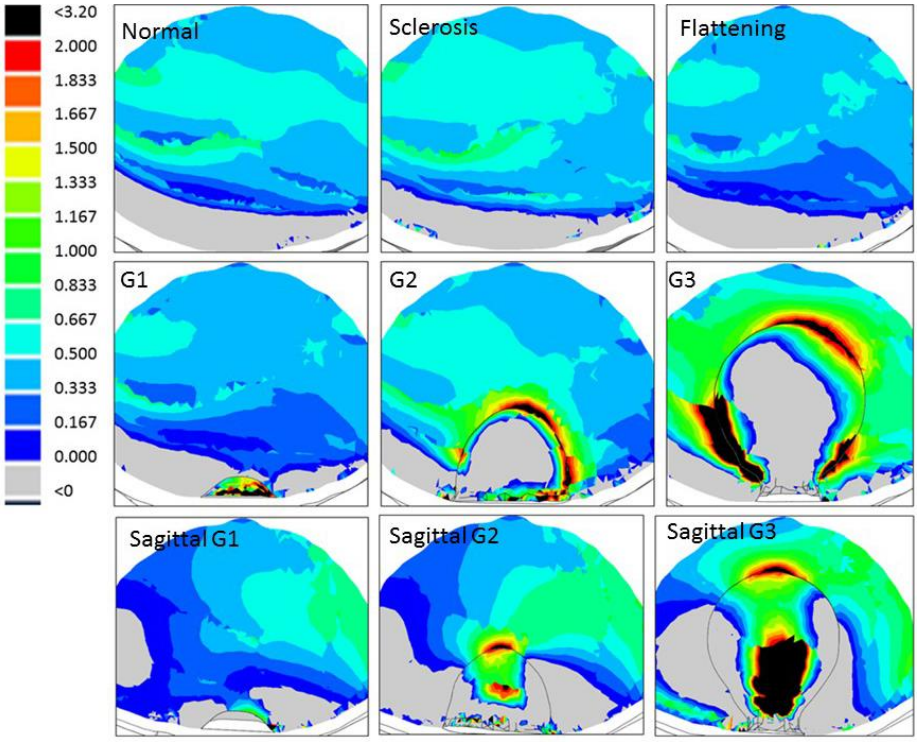

Figure 3.10 Tension stress maps in MPa for MFC. The first six maps are for frontal plane tension, and the last three for sagittal plane tension. The first three conditions (normal, sclerosis and flattening) for the sagittal plane were almost identical to the frontal plane and are omitted. The point of view for the frontal plane is caudal to cranial (medial is right of image) and for the sagittal plane is medial to lateral (cranial is right of image). Tensions are significantly elevated in the G2 and G3 defects compared with the Normal condition.

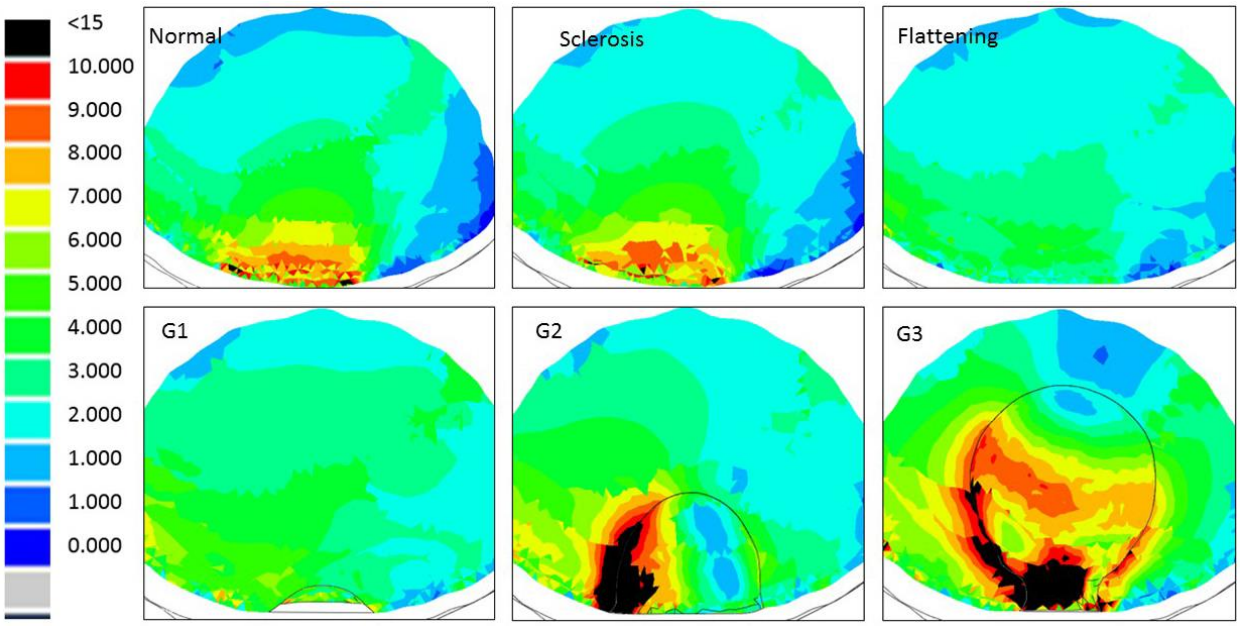

Figure 3.11 Shear stress maps in MPa for MFC for all six conditions in the frontal plane. The point of view is caudal to cranial (medial is right of image). Shear stresses are high at the articulation site with the Normal and Sclerotic conditions. Shear stresses are lowered in the Flattening and G1 conditions. Shear stresses are then elevated cranial and lateral with G2 and G3 defects.

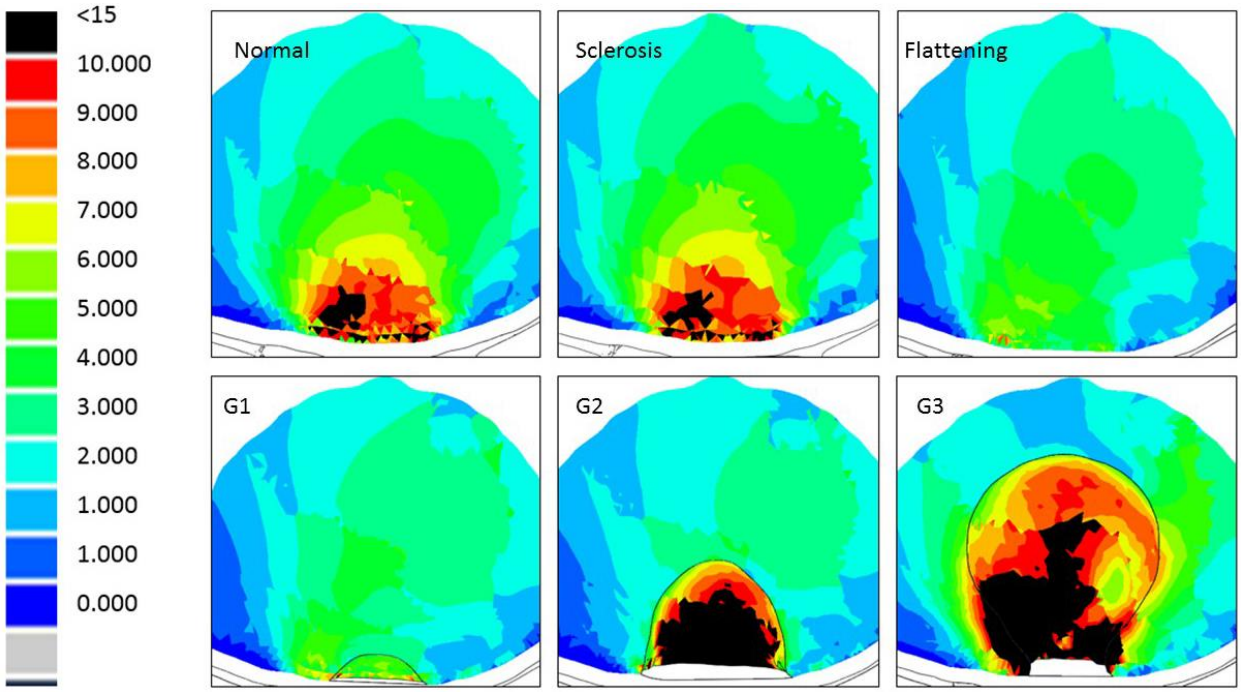

Figure 3.12 Shear stress maps in MPa for MFC for all six conditions in the sagittal plane. The point of view is medial to lateral (cranial is right of image). High shear stress is observed at the articulation region in the Normal and Sclerotic conditions. Shear stresses decreased in the Flattened and the G1 defect conditions. Shear stresses are then increased substantially in the G2 and G3 defects lateral to the cyst.

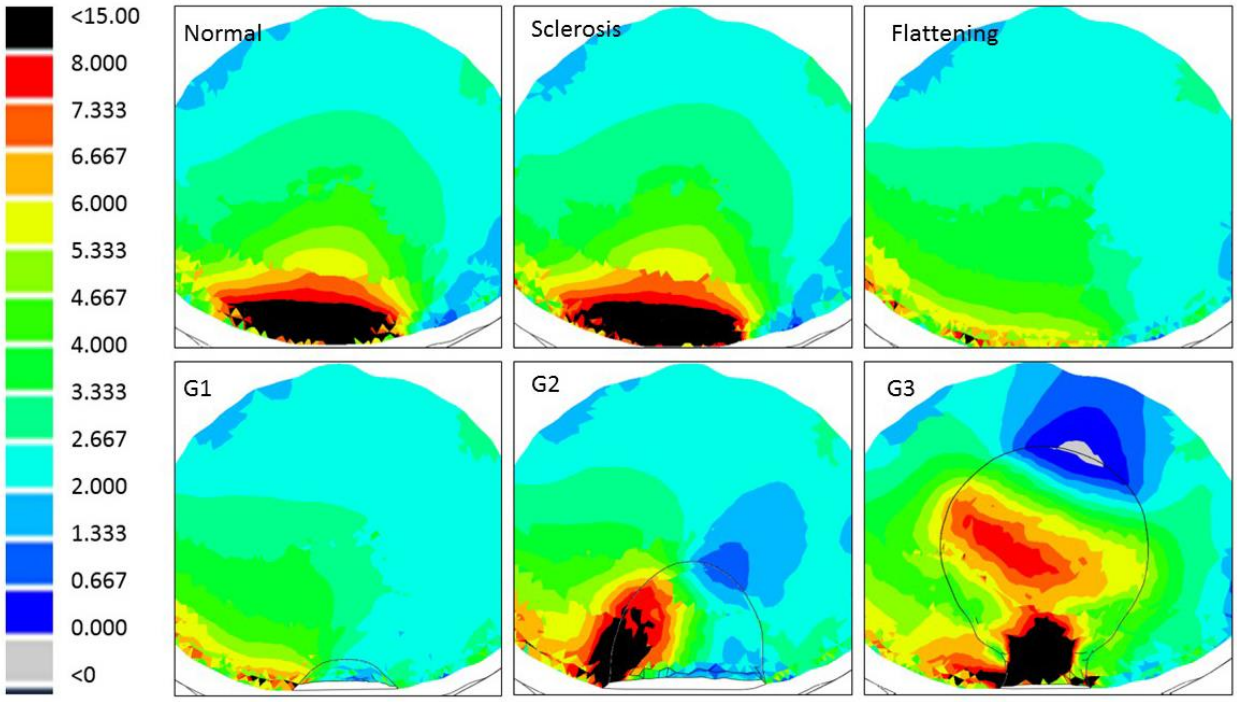

Figure 3.13 Compression stress maps in MPa for all six conditions in the frontal plane. The point of view is caudal to cranial (medial is right of image). Compressions are high at the articulation region in the Normal and Sclerotic conditions. A decrease is observed in the Flattened and G1 conditions. Compressive stresses are then elevated cranial and lateral to the cystic structures in the G2 and G3 conditions.

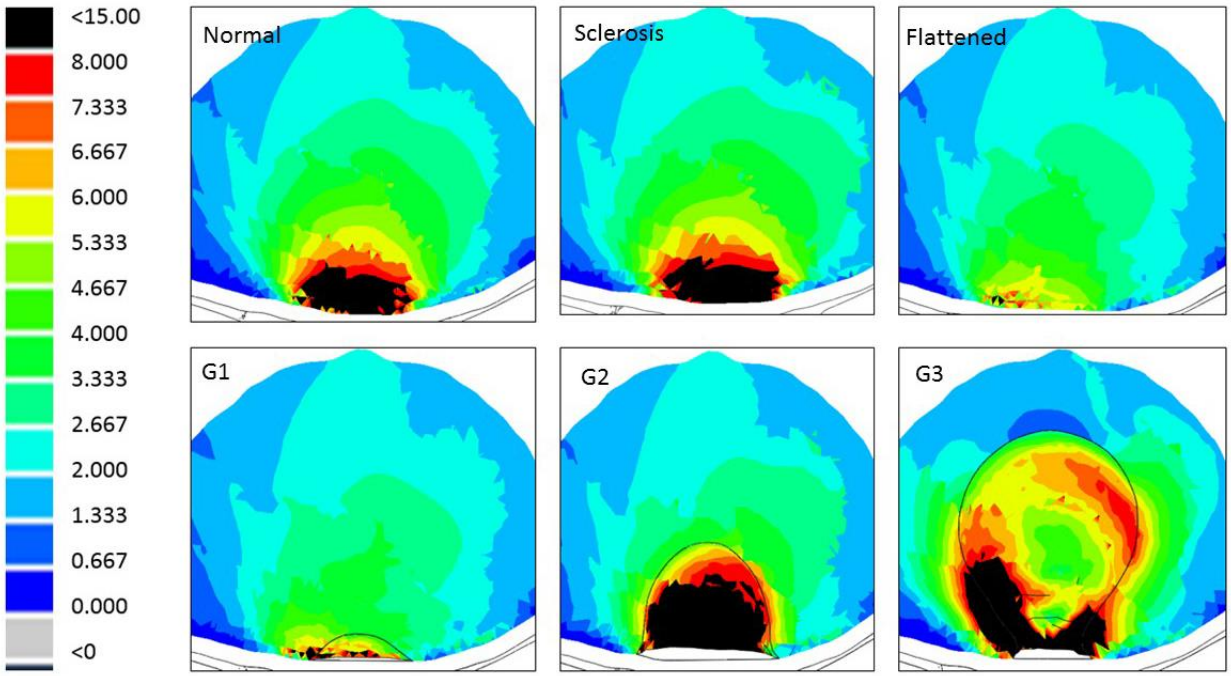

Figure 3.14 Compression stress maps in MPa for all six conditions in the sagittal plane. The point of view is medial to lateral (cranial is right of image). High compressions are observed at the articulation site in the Normal and Sclerotic conditions. Compressive stresses decrease in the Flattened and G1 conditions. Increases in compressive stress (over normal) occur in the G2 and G3 conditions, most notably lateral to the cyst and in the necking region of the G3 defect.

3.4. Discussion

Finite element models can provide researchers and clinicians alike with a powerful tool to study biological phenomena that would otherwise be impossible to study. With careful implementation of appropriate boundary conditions and material properties, finite element analysis provides an accurate representation of what is likely to be found experimentally, if we had the necessary equipment to do so. The purpose of this study was to utilize a finite element model of an equine stifle joint to better understand the biomechanical consequences of SCL in the MFC.

In a previous finite element study, McErlain et al. demonstrated that von Mises stresses are elevated in bone adjacent to an idealized spherical SCL (cyst) in knees of osteoarthritis patients [24]. However, von Mises stresses do not provide a full mechanical picture, especially in biological tissue such as bone. Our study investigated the tensile, compressive, shear stresses, as well as von Mises stresses associated with SCL in the equine stifle. We also expanded the region of interest to encapsulate changes for several millimeters on the periphery of the SCL, whereas Mcerlain only considered a 1 mm layer for the stresses. Also worth noting, compared with McErlain et al.'s findings, we found that von Mises stresses, along with compressive and shear stresses, actually decreased in defects of smaller size (<0.5 cm^3) (Table 3.3). This has implications on treatment strategies depending on the severity of the defect.

The stress data presented in this study offer new insight into subchondral lesion development. The large increases in tension, especially with the G2 and G3 defects, are startling when considering that trabecular bone is weak in tension and shear, and that *in vivo* loads at a galloping pace are higher than those tested in this model. This increase in tension, coupled with continued loading, would not provide an environment conducive to healthy bone

healing/remodeling. However, increased tension also indicates an increase in strain (leading to microfractures and damage that must be healed).

Perhaps the most surprising finding is the significant drop in compressive and shear stresses with the flattened and G1 condition. However, considering that flattening the femur increases the contact area with the tibial plateau, peak stresses should decrease as the load can now be transferred across a greater surface. Bone resorption may explain how a defect forms after a flattening of the femur. The significant drop in stresses at the articulation site may lead to a bone adaptation. However, it is more likely that bone damage is present after a flattening occurs, and a defect forms as a response to this trabecular damage, which cannot be healed under continued loading.

To the author's knowledge, this is the first study that examined the mechanical impact of a flattened articular surface on the MFC and of various sizes of SCLs. Flattening the MFC increased stress in all three SCL models, most notably tension. It should be noted that only the bone on the medial femoral condyle was flattened. This resulted in a gap between the femur and the tibia not present in the non-flattened models. It took roughly 400 N of force to fully close the gap, thus transmitting more of the force to the lateral tibial plateau. Stresses may have been further exacerbated if the two bones began in contact. Unfortunately, the lack of data available make this idealized flattening the most reasonable assumption. When high-resolution 3D image data of a flattened femur become available, future models will incorporate that geometry.

There are a number of limitations associated with the study. Only one CT image set was used, and thus we cannot determine if some of our results are specific to the stifle geometry used to create our model. Also, the flattening of the femur and the SCL placement was idealized based

on clinical observations. Ideally, a horse stifle would be imaged over a course of time to capture the healthy and damaged states, and model geometries would be made accordingly. We have also artificially constrained the model by not allowing internal and external rotation. Lastly, the model does not include any damaged bone, something that is likely present after flattening and before subchondral lesions begin to manifest, especially if the trabecular bone is collapsing to allow for a flattened femur. With the lack of data available on bone quality around SCLs, it did not seem reasonable to include changes in bone properties outside of sclerosis. Future studies will address these limitations.

SCL development in the MFC is likely a multifaceted phenomenon. However, the mechanical data from this model suggests that altered stresses in the MFC is a major factor in SCL development. It also suggests that treatment of a SCL in the MFC should address alterations in MFC biomechanics as proposed by Santschi et al.[9]. This study also has significant implications for human orthopedic disease. Humans develop SCLs, most typically as a bone "adaptation" during the onset of osteoarthritis [37-39]. Gregory et al. discuss the relevance of certain animal models, such as the horse, functioning as a reliable platform to translate animal research into human implications [40]. Typically, mouse models are used, but they lack the anatomical similarity to humans [41]. With horse stifles being anatomically similar to human knees, and because equine SCLs occur without the confounding effects of osteoarthritis, our model has advantages for the study of human SCLs.

In conclusion, a finite element model of an equine stifle joint was developed in order to study the biomechanical consequences of SCL in the MFC. We found that significant stress changes occur in the MFC during SCL development, resulting in a positive feedback loop that perpetuates and grows the SCL. Appropriate treatments of SCLs that restore the mechanical

environment of the MFC should help to promote bone healing. Future models will add a transcondylar screw to the model to investigate the impact of the screw and its placement on MFC biomechanics.

3.5. References

[1] Jeffcott, L. B., and Kold, S. E., 1982, "Clinical and Radiological Aspects of Stifle Bone Cysts in the Horse," Equine Veterinary Journal, 14(1), pp. 40-46.

[2] Stewart, B., and Reid, C. F., 1982, "Osseous Cyst-Like Lesions of the Medial Femoral Condyle in the Horse," J Am Vet Med Assoc, 180(3), pp. 254-7.

[3] Mcilwraith, C. W., 1982, "Subchondral Cystic Lesions (Osteochondrosis) in the Horse," Compend Contin Educ Pract Vet, 4(pp. s282-s294.

[4] Baxter, G., 1996,

[5] Jeffcott, L. B., Kold, S. E., and Melsen, F., 1983, "Aspects of the Pathology of Stifle Bone Cysts in the Horse," Equine Vet J, 15(4), pp. 304-11.

[6] White, N. A., Mcilwraith, C. W., and Allen, D., 1988, "Curettage of Subchondral Bone Cysts in Medial Femoral Condyles of the Horse," Equine Veterinary Journal, 20(pp. 120-124.

[7] Svon Rechenberg, B., Leutenegger, C., Zlinsky, K., Mcilwraith, C. W., Akens, M. K., and Auer, J. A., 2001, "Upregulation of Mrna of Interleukin-1 and -6 in Subchondral Cystic Lesions of Four Horses," Equine Veterinary Journal, 33(2), pp. 143-149.

[8] Von Rechenberg, B., Guenther, H., Mcilwraith, C. W., Leutenegger, C., Frisbie, D. D., Akens, M. K., and Auer, J. A., 2000, "Fibrous Tissue of Subchondral Cystic Lesions in Horses Produce Local Mediators and Neutral Metalloproteinases and Cause Bone Resorption in Vitro," Vet Surg, 29(5), pp. 420-9.

[9] Santschi, E. M., Williams, J. M., Morgan, J. W., Johnson, C. R., Bertone, A. L., and Juzwiak, J. S., 2015, "Preliminary Investigation of the Treatment of Equine Medial Femoral Condylar Subchondral Cystic Lesions with a Transcondylar Screw," Vet Surg, 44(3), pp. 281-8.

[10] Wallis, T. W., Goodrich, L. R., Mcilwraith, C. W., Frisbie, D. D., Hendrickson, D. A., Trotter, G. W., Baxter, G. M., and Kawcak, C. E., 2008, "Arthroscopic Injection of Corticosteroids into the Fibrous Tissue of Subchondral Cystic Lesions of the Medial Femoral Condyle in Horses: A Retrospective Study of 52 Cases (2001-2006)," Equine Vet J, 40(5), pp. 461-7.

[11] Howard, R. D., Mcilwraith, C. W., and Trotter, G. W., 1995, "Arthroscopic Surgery for Subchondral Cystic Lesions of the Medial Femoral Condyle in Horses: 41 Cases (1988-1991)," J Am Vet Med Assoc, 206(6), pp. 842-50.

[12] Lewis, R., 1987,

[13] Smith, M. A., Walmsley, J. P., Phillips, T. J., Pinchbeck, G. L., Booth, T. M., Greet, T. R., Richardson, D. W., Ross, M. W., Schramme, M. C., Singer, E. R., Smith, R. K., and Clegg, P. D., 2005, "Effect of Age at Presentation on Outcome Following Arthroscopic Debridement of Subchondral Cystic Lesions of the Medial Femoral Condyle: 85 Horses (1993--2003)," Equine Vet J, 37(2), pp. 175-80.

[14] Bodo, G., Hangody, L., Modis, L., and Hurtig, M., 2004, "Autologous Osteochondral Grafting (Mosaic Arthroplasty) for Treatment of Subchondral Cystic Lesions in the Equine Stifle and Fetlock Joints," Vet Surg, 33(6), pp. 588-96.

[15] Ortved, K. F., Nixon, A. J., Mohammed, H. O., and Fortier, L. A., 2012, "Treatment of Subchondral Cystic Lesions of the Medial Femoral Condyle of Mature Horses with Growth Factor Enhanced Chondrocyte Grafts: A Retrospective Study of 49 Cases," Equine Vet J, 44(5), pp. 606-13.

[16] Jj, F., 2006, "Injection of Equine Subchondral Bone Cysts with Triamcinolone: 73 Horses (1999-2005)," eds., 52, pp. 412-413.

[17] Brommer, H., Brama, P. A., Laasanen, M. S., Helminen, H. J., Van Weeren, P. R., and Jurvelin, J. S., 2005, "Functional Adaptation of Articular Cartilage from Birth to Maturity under the Influence of Loading: A Biomechanical Analysis," Equine Vet J, 37(2), pp. 148-54.

[18] Diamant, I., Shahar, R., and Gefen, A., 2005, "How to Select the Elastic Modulus for Cancellous Bone in Patient-Specific Continuum Models of the Spine," Medical and Biological Engineering and Computing, 43(4), pp. 465-472.

[19] Hodgskinson, R., and Currey, J. D., 1992, "Young's Modulus, Density and Material Properties in Cancellous Bone over a Large Density Range," Journal of Materials Science: Materials in Medicine, 3(5), pp. 377-381.

[20] Mah, P., Reeves, T. E., and Mcdavid, W. D., 2010, "Deriving Hounsfield Units Using Grey Levels in Cone Beam Computed Tomography," Dentomaxillofac Radiol, 39(6), pp. 323-35.

[21] Seong, W.-J., Kim, U.-K., Swift, J. Q., Heo, Y.-C., Hodges, J. S., and Ko, C.-C., 2009, "Elastic Properties and Apparent Density of Human Edentulous Maxilla and Mandible," International journal of oral and maxillofacial surgery, 38(10), pp. 1088-1093.

[22] Donahue, T. L. H., Hull, M. L., Rashid, M. M., and Jacobs, C. R., 2003, "How the Stiffness of Meniscal Attachments and Meniscal Material Properties Affect Tibio-Femoral Contact Pressure Computed Using a Validated Finite Element Model of the Human Knee Joint," J Biomech, 36(1), pp. 19-34.

[23] Kiapour, A., Kiapour, A. M., Kaul, V., Quatman, C. E., Wordeman, S. C., Hewett, T. E., Demetropoulos, C. K., and Goel, V. K., 2014, "Finite Element Model of the Knee for Investigation of Injury Mechanisms: Development and Validation," J Biomech Eng, 136(1), pp. 011002.

[24] Mcerlain, D. D., Milner, J. S., Ivanov, T. G., Jencikova-Celerin, L., Pollmann, S. I., and Holdsworth, D. W., 2011, "Subchondral Cysts Create Increased Intra-Osseous Stress in Early Knee Oa: A Finite Element Analysis Using Simulated Lesions," Bone, 48(3), pp. 639-46.

[25] Mootanah, R., Imhauser, C. W., Reisse, F., Carpanen, D., Walker, R. W., Koff, M. F., Lenhoff, M. W., Rozbruch, S. R., Fragomen, A. T., Dewan, Z., Kirane, Y. M., Cheah, K., Dowell, J. K., and Hillstrom, H. J., 2014, "Development and Validation of a Computational Model of the Knee Joint for the Evaluation of Surgical Treatments for Osteoarthritis," Comput Methods Biomech Biomed Engin, 17(13), pp. 1502-17.

[26] Papaioannou, G., Demetropoulos, C. K., and King, Y. H., 2010, "Predicting the Effects of Knee Focal Articular Surface Injury with a Patient-Specific Finite Element Model," The Knee, 17(1), pp. 61-68.

[27] Pena, E., Calvo, B., Martinez, M. A., and Doblare, M., 2006, "A Three-Dimensional Finite Element Analysis of the Combined Behavior of Ligaments and Menisci in the Healthy Human Knee Joint," J Biomech, 39(9), pp. 1686-701.

[28] Yao, J., Funkenbusch, P. D., Snibbe, J., Maloney, M., and Lerner, A. L., 2006, "Sensitivities of Medial Meniscal Motion and Deformation to Material Properties of Articular Cartilage, Meniscus and Meniscal Attachments Using Design of Experiments Methods," J Biomech Eng, 128(3), pp. 399-408.

[29] Anderson, A. E., Peters, C. L., Tuttle, B. D., and Weiss, J. A., 2005, "Subject-Specific Finite Element Model of the Pelvis: Development, Validation and Sensitivity Studies," J Biomech Eng, 127(3), pp. 364-73.

[30] Ellis, B. J., Debski, R. E., Moore, S. M., Mcmahon, P. J., and Weiss, J. A., 2007, "Methodology and Sensitivity Studies for Finite Element Modeling of the Inferior Glenohumeral Ligament Complex," J Biomech, 40(3), pp. 603-12.

[31] Henninger, H. B., Reese, S. P., Anderson, A. E., and Weiss, J. A., 2010, "Validation of Computational Models in Biomechanics," Proc Inst Mech Eng H, 224(7), pp. 801-12.

[32] Weiss, J. A., Gardiner, J. C., Ellis, B. J., Lujan, T. J., and Phatak, N. S., 2005, "Three-Dimensional Finite Element Modeling of Ligaments: Technical Aspects," Medical Engineering & Physics, 27(10), pp. 845-861.

[33] Jones, A. C., and Wilcox, R. K., 2008, "Finite Element Analysis of the Spine: Towards a Framework of Verification, Validation and Sensitivity Analysis," Med Eng Phys, 30(10), pp. 1287-304.

[34] Bonilla, A. G., Williams, J. M., Litsky, A. S., and Santschi, E. M., 2015, "Ex Vivo Equine Medial Tibial Plateau Contact Pressure with an Intact Medial Femoral Condyle, with a Medial Femoral Condylar Defect, and after Placement of a Transcondylar Screw through the Condylar Defect," Vet Surg, 44(3), pp. 289-96.

[35] Munoz-Nates, F., Chateau, H., Van Hamme, A., Camus, M., Pauchard, M., Ravary-Plumioen, B., Denoix, J. M., Pourcelot, P., and Crevier-Denoix, N., 2015, "Accelerometric and Dynamometric Measurements of the Impact Shock of the Equine Forelimb and Hindlimb at High Speed Trot on Six Different Tracks - Preliminary Study in One Horse," Comput Methods Biomech Biomed Engin, 18 Suppl 1(pp. 2012-3.

[36] 2002, "Addendum: Pqct as an Investigation Tool," Acta Orthopaedica Scandinavica, 73(2), pp. 44-52.

[37] Audrey, H. X., Abd Razak, H. R., and Andrew, T. H., 2014, "The Truth Behind Subchondral Cysts in Osteoarthritis of the Knee," Open Orthop J, 8(pp. 7-10.

[38] Goldring, M. B., and Goldring, S. R., 2010, "Articular Cartilage and Subchondral Bone in the Pathogenesis of Osteoarthritis," Annals of the New York Academy of Sciences, 1192(1), pp. 230-237.

[39] Goldring, S. R., 2008, "The Role of Bone in Osteoarthritis Pathogenesis," Rheumatic Disease Clinics of North America, 34(3), pp. 561-571.

[40] Gregory, M. H., Capito, N., Kuroki, K., Stoker, A. M., Cook, J. L., and Sherman, S. L., 2012, "A Review of Translational Animal Models for Knee Osteoarthritis," Arthritis, 2012(pp. 14.

[41] Guzman, R. E., Evans, M. G., Bove, S., Morenko, B., and Kilgore, K., 2003, "Mono-Iodoacetate-Induced Histologic Changes in Subchondral Bone and Articular Cartilage of Rat Femorotibial Joints: An Animal Model of Osteoarthritis," Toxicol Pathol, 31(6), pp. 619-24.

Conclusion / Future Work

Chapter one of this Thesis addressed the severity of subchondral bone cysts in the medial femoral condyle of the horse. Both the large population affected, as well as the implications on horse health make the full understanding of SBC pathogenesis high priority. With an understanding of its pathology, rational treatment strategies can be implemented, ultimately raising the low percentage of success rates in current treatment strategies. Interestingly enough, humans suffer from the same cystic lesions, most often in conjunction with osteoarthritis. With horses having an anatomically similar joint compared to the human knee, experiencing the proportional loads as a human knee, and having SBCs without osteoarthritis, the horse model is advantageous to the study of human SBCs, as well.

A critical obstacle facing clinicians in the study of SBCs is that the defect is subchondral, making it incredibly difficult to study in a live horse. Chapter one discussed the advantage of using finite element analysis to overcome this obstacle.

It is hypothesized that SBCs create serious mechanical consequences in the surrounding bone, providing an unfavorable environment for the bone to undergo healthy remodeling. This constant state of elevated stresses coupled with constant loading may explain cyst growth and development. Thus, this work aimed to test that hypothesis by creating a finite element model of an equine stifle joint and investigating stresses at each stage of cystic progression.

Chapter two focused on the development of an equine stifle model, as well as providing insight into the general process of computational modeling. This insight focused on the importance of understanding how the desired output of a model dictates what assumptions can be made in the inputs (material properties, boundary conditions, structure omissions, etc). For

example, the equine stifle joint needed to produce accurate stresses within the bone of the medial femoral condyle. Thus, the way the condyle interacts with the tibial plateau is especially important as this is the site of load transfer. Accordingly, the way the meniscus interacts with the tibial plateau has significant effect on the stresses recorded. Thus, spring attachments were utilized to allow for semi-constrained interaction, as opposed to a simpler tie interaction. On the other hand, a reported range of cartilage properties in the literature had little effect on the Von Mises stresses within the bone of the condyle. This insensitivity of cartilage properties on Von Mises stresses could allow for any reported value to be used, as long as Von Mises stresses were of primary concern. Chapter two also demonstrates the importance of mesh convergence and how convergence for one variable does not guarantee convergence for another variable. For example, it was found that for an output of Von Mises stresses, convergence was demonstrated at a much coarser mesh than was demonstrated for maximum principal stress. Therefore, a mesh refinement should be made in light of convergence for every output. Ultimately, a verified model of the equine stifle joint was developed. Validation, beyond proper selection of material properties, was demonstrated in chapter three.

Chapter three implemented the equine stifle model to address the biomechanics associated with subchondral bone cysts. It was found that significant changes in the femoral bone occur in each stage of cystic progression (beginning with bone sclerosis and ending in a severe defect). Most notably, tensions increase in a severe defect by more than 100% compared to a healthy, intact femur. Increased tension alongside continued loading may prevent the bone from healing properly, and ultimately resulting in further growth of the defect. Other modes of stress such as shear and compression decreased with smaller defects. This may suggest an adaptation could occur in which an increase in bone resorption further destroys the bone. However, it is

more likely that a defect occurs after flattening due to a damage repair response. This work has provided new, critical insight into the role that biomechanics have in SBCs, and provide rationale in implementing treatments that address the mechanical changes in the bone.

Though this work has a significant impact in the clinical sciences, several limitations exist and can be addressed in future work. These limitations and how future work can address them include:

Limitation: A single CT image set was used to create all models used in this work. The image data belonged to a healthy stifle joint, and thus all stages of the cystic development process were idealized.

Future Work: Additional image sets can be obtained to create more models. With more models analyzed, the possibility of subject-specific geometries having a significant impact on femoral bone stresses can be examined. Also, if image data of a horse with a SBC is obtained, a defect model can be made based on the native geometry.

Limitation: The current model is only able to provide an instantaneous stress response in one orientation (full extension), neglecting the effect of long-term, repetitive loading with multiple stifle orientations.

Future Work: Kinematic data of an equine stifle in a moving horse could be used as loading/boundary conditions to create a dynamic model. Material properties could be changed accordingly. This process could also be idealized by analyzing quasi-static models in other joint orientations. Creating an axis of rotation in the femur, the joint can be flexed and extended to different flexion angles for the loaded part of gait. At each flexion angle, the appropriate load

could then be applied, and the process could be repeated several times. ABAQUS can handle this type of loading using multiple loading steps.

Limitation: Bone damage was not addressed in this model, nor was there a criteria set to create bone damage.

Future Work: A critical examination of literature could be performed to gain any insight into the quality of the bone surrounding a subchondral lesion and/or the quality of bone in flattened femurs. Lowering the properties of the bone to account for damage might be more realistic for of SBC modeling the flattened femur and cyst development. Also, using a criteria for bone adaptation, such as Wolff's Law, an iterative modeling scheme could be employed to predict the response of bone to damage and stresses leading to cyst growth or healing.

Beyond the future work highlighted to address the study limitations, future models should examine cyst stress before and after a screw is inserted into the model. These will help us understand the efficacy of this surgical treatment that is mechanically focused. In summary, treatments such as that proposed by Santschi et al. should be thoroughly investigated.

Appendix

```
%% Lance Frazer
% m.file used for Master's work
% April 29th, 2016

%% Extracting Data from ABAQUS
% 1. Under the report tab, create rpt. file
% 2. Open rpt. file in Excel
% 3. Move dividers so that:
    % C Column is Von Mises stress
    % D Column is maximum principal stress
    % G Column is minimum principal stress
    % H Column is Tresca stress
% 4. Save as Excel file

%% Reading in Data
clear all;
clc;

WorkBook = 'Normal-EN'; % CHANGE Excel file name
disp(WorkBook)

%% Obtaining Tensions (Positive Maximum Principal Stresses)

[D Y A] = xlsread(WorkBook,1,'A20:A1000000'); % Change range if nec.
[C X Data] = xlsread(WorkBook,1,'D20:D1000000'); % Change range if nec.

for i = 20:1000000 % Change range if nec.
    if ischar(A{i-19}) == 1 % If cell in A column is a string
        Data{i-19} = 0; % Changes the corresponding C cell to 0
    end
end

emptycells = cellfun(@isempty,Data); % Finds empty cells
Data(emptycells) = []; % Deletes empty cells

b = cellfun(@isnan,Data); % Finds NaN entries
idx = find(b(:,1));
Data(idx,:) = []; % Deletes NaN entries

Data = cell2mat(Data); % Converts cell array to matrix
Data(Data == 0) = []; % Deletes zeroes made from the above for loop

Signs = sign(Data);
for j = 1:length(Signs) % Finds positives and negatives
    if Signs(j) == 1
        Tensions(j) = Data(j); % Positives = Tensions
    else
        Compressions(j) = Data(j); % Negatives = Compressions
    end
end

Tensions(Tensions == 0) = []; % Deletes zeroes created from sign for loop
```

```
Top5Tension = prctile(Tensions,95)
clearvars -except WorkBook

%% Obtaining Compressions (Negative Minimum Principal Stresses)

[D Y A] = xlsread(WorkBook,1,'A20:A1000000'); % Change range if nec.
[C X Data] = xlsread(WorkBook,1,'G20:G1000000'); % Change range if nec.

for i = 20:1000000 % Change range if nec.
    if ischar(A{i-19}) == 1 % If cell in A column is a string
        Data{i-19} = 0; % Changes the corresponding C cell to 0
    end
end

emptycells = cellfun(@isempty,Data); % Finds empty cells
Data(emptycells) = []; % Deletes empty cells

b = cellfun(@isnan,Data); % Finds NaN entries
idx = find(b(:,1));
Data(idx,:) = []; % Deletes NaN entries

Data = cell2mat(Data); % Converts cell array to matrix
Data(Data == 0) = []; % Deletes zeroes made from the above for loop

Signs = sign(Data);
for j = 1:length(Signs) % Finds positives and negatives
    if Signs(j) == 1
        Tensions(j) = Data(j); % Positives = Tensions
    else
        Compressions(j) = Data(j); % Negatives = Compressions
    end
end

Compressions(Compressions == 0) = [];

Top5Compression = -prctile(-Compressions,95)

clearvars -except WorkBook

%% Obtaining Von Mises Stresses

[D Y A] = xlsread(WorkBook,1,'A20:A1000000'); % Change range if nec.
[C X Data] = xlsread(WorkBook,1,'C20:C1000000'); % Change range if nec.

for i = 20:1000000 % Change range if nec.
    if ischar(A{i-19}) == 1 % If cell in A column is a string
        Data{i-19} = 0; % Changes the corresponding C cell to 0
    end
end

emptycells = cellfun(@isempty,Data); % Finds empty cells
Data(emptycells) = []; % Deletes empty cells
```

```
b = cellfun(@isnan,Data); % Finds NaN entries
idx = find(b(:,1));
Data(idx,:) = []; % Deletes NaN entries

Data = cell2mat(Data); % Converts cell array to matrix
Data(Data == 0) = []; % Deletes zeroes made from the above for loop

VM = Data;

Top5VM = prctile(VM,95)
clearvars -except WorkBook
%% Obtaining Tresca Stresses (Maximum Shear Stresses)

[D Y A] = xlsread(WorkBook,1,'A20:A1000000'); % Change range if nec.
[C X Data] = xlsread(WorkBook,1,'H20:H1000000'); % Change range if nec.

for i = 20:1000000 % Change range if nec.
    if ischar(A{i-19}) == 1 % If cell in A column is a string
        Data{i-19} = 0; % Changes the corresponding C cell to 0
    end
end

emptycells = cellfun(@isempty,Data); % Finds empty cells
Data(emptycells) = []; % Deletes empty cells

b = cellfun(@isnan,Data); % Finds NaN entries
idx = find(b(:,1));
Data(idx,:) = []; % Deletes NaN entries

Data = cell2mat(Data); % Converts cell array to matrix
Data(Data == 0) = []; % Deletes zeroes made from the above for loop

Tresca = Data;

Top5Tresca = prctile(Tresca,95)
```